



ELSEVIER

Biochimica et Biophysica Acta 1458 (2000) 482–510



www.elsevier.com/locate/bba

Review

Reverse engineering a protein: the mechanochemistry of ATP synthase

George Oster *, Hongyun Wang

Department of Molecular and Cellular Biology and College of Natural Resources, University of California, Berkeley, CA 94720-3112, USA

Received 19 April 1999; received in revised form 26 July 1999; accepted 5 August 1999

Abstract

ATP synthase comprises two rotary motors in one. The F_1 motor can generate a mechanical torque using the hydrolysis energy of ATP. The F_o motor generates a rotary torque in the opposite direction, but it employs a transmembrane proton motive force. Each motor can be reversed: The F_o motor can drive the F_1 motor in reverse to synthesize ATP, and the F_1 motor can drive the F_o motor in reverse to pump protons. Thus ATP synthase exhibits two of the major energy transduction pathways employed by the cell to convert chemical energy into mechanical force. Here we show how a physical analysis of the F_1 and F_o motors can provide a unified view of the mechanochemical principles underlying these energy transducers. © 2000 Elsevier Science B.V. All rights reserved.

Keywords: ATP synthase; Bioenergetics; Mechanochemistry; Modeling; ATP Hydrolysis

1. Introduction

ATP synthase is unique amongst proteins in that it embodies two of the major cellular energy transduction mechanisms. F_1 can synthesize ATP, but it can also hydrolyze ATP to operate as a motor. F_o can convert a transmembrane ion gradient into a rotary torque, or it can be driven in reverse to perform as an ion pump. As the content of this volume attests, we now know a great deal about the structure, biochemistry, genetics, and energetics of ATP synthase. An important missing piece in the story of this extraordinary protein is an understanding of the basic physical principles that underlie its operation.

This growing body of knowledge has stimulated several workers in the field to offer qualitative scenarios for the mechanisms of both F_1 and F_o . However, there is no way to know which, if any, of these scenarios are consistent with the laws of chemistry and physics, nor to make quantitative predictions to compare with experiments. Therefore, we set about trying to construct a quantitative model for both F_1 and F_o that would encapsulate the current state of experimental knowledge and provide insight into the fundamental mechanisms by which ATP synthase operates.

The models are formulated as equations that are solved on a computer. A detailed account of these calculations can be found in the supplemental material to the published papers [1–3]; calculations not given in these references are included here as appendices. In this review we endeavor to present an intuitive account of how the models were constructed and clearly delineate our assumptions and why we made them. Of course, different assumptions are

* Corresponding author. Fax: +1-510-642-7428;
E-mail: goster@nature.berkeley.edu

possible, and so the models were constructed so as to handle alternate hypotheses, such as different kinetics or structures. In this way the models can serve as vehicles for testing various hypotheses against new experimental information as it becomes available.

In this review we will also introduce an important new aspect to the F_1 model which is a consequence of its high mechanical efficiency. We will show that the mechanical and kinetic data require that the power stroke that drives rotation must derive its energy from the binding of ATP to the catalytic sites. Further, this binding transition must take place gradually from weak to tight. We call this process the ‘Binding Zipper’. The energy from hydrolysis of the γ -phosphate bond is used to weaken the tight binding so the products can be released and the cycle can repeat. We will see that a mechanochemical cycle built around the Binding Zipper unifies many of the experimental findings on the F_1 motor.

Fig. 1 shows the overall geometry of ATP synthase. The F_1 motor/synthetase consists of subunits $\alpha_3\beta_3\gamma\epsilon$. The F_0 motor/pump consists of subunits $c_{12}ab_2\delta$. A more functional breakdown of the subunits arises from the realization by Boyer, and the unequivocal demonstration by the laboratories of Yoshida and Kinosita, that F_1 is a rotary machine [4–7]. The rotational motion of the F_0 motor had been inferred from the cylindrical organization of the c_{12} subunit, and the fact that it is connected to F_1 by the $\gamma\epsilon$ shaft. However, recent experiments have directly confirmed that the c_{12} subunit rotates with the γ shaft (M. Yoshida, personal communication). Thus the convention has arisen to refer to the counter-rotating subunit collections $\gamma\epsilon c_{12}$ and $ab_2\delta\alpha_3\beta_3$ as the ‘rotor’ and ‘stator’, respectively. Because both F_1 and F_0 are rotary motors, we can analyze their mechanochemical coupling more easily than other protein motors whose motions are more complicated.

2. The F_1 motor

The experiments of Yoshida’s and Kinosita’s laboratories provided a striking visual confirmation of the rotary motion of the F_1 motor [7]. Equally as important from the viewpoint of modeling, they es-

tablished the following characteristics of the F_1 motor [6]:

- The motor rotated in three steps per revolution; rotation was stochastic, with occasional backward steps.
- Each step corresponded to the hydrolysis of one ATP.
- At high ATP concentration, the viscous dissipation per revolution as computed from the mean velocity was about the same as the free energy of hydrolyzing three ATPs. This means that, *at these conditions, the energy conversion efficiency from nucleotide hydrolysis to rotary torque is close to 100%*. Consequently, there must be very tight coupling between the mechanics and the chemistry so that entropic losses are small. This high efficiency also implies that *the rotary torque generated is nearly constant*. Because this amazing result informs nearly every step in constructing the model, it merits a more detailed explanation, which we give in Appendix A.

In constructing the model we proceed sequentially as follows. First, we must establish the geometrical motions the F_1 subunits undergo (‘kinematics’). Then we introduce the mechanical forces that drive the conformational changes (‘dynamics’). Next, we model the chemical reactions that provide the energy that generates the forces. Finally we show how the chemistry and mechanics are coordinated so as to achieve the high energy conversion efficiency observed in the experiments.

The form of the equations that constitute the model are very simple. Let $\theta(t)$ denote the angular position of the γ subunit at time t , and let $\mathbf{s}(t)$ denote the ‘chemical state’ of F_1 at the same instant. By this we mean the occupancy of the three catalytic sites (**Empty**, **ATP**, **ADP•P_i**, **ADP**). Then the mechanical balance of torques on the γ shaft is:

$$\underbrace{\zeta \frac{d\theta}{dt}}_{\text{Viscous drag}} = \underbrace{\sum_{\beta=1}^3 \tau_H^\beta(\theta, \mathbf{s})}_{\text{Torque generated by nucleotide hydrolysis}} + \underbrace{\tau_B(t)}_{\text{Brownian torque}} \quad (1)$$

Here ζ is a viscous drag coefficient, $\tau_B(t)$ is the torque due to Brownian motion, and the three torques, $\tau_H^\beta(\theta, \mathbf{s})$, are developed at the F_1 catalytic sites during the nucleotide hydrolysis cycle. This mechanical

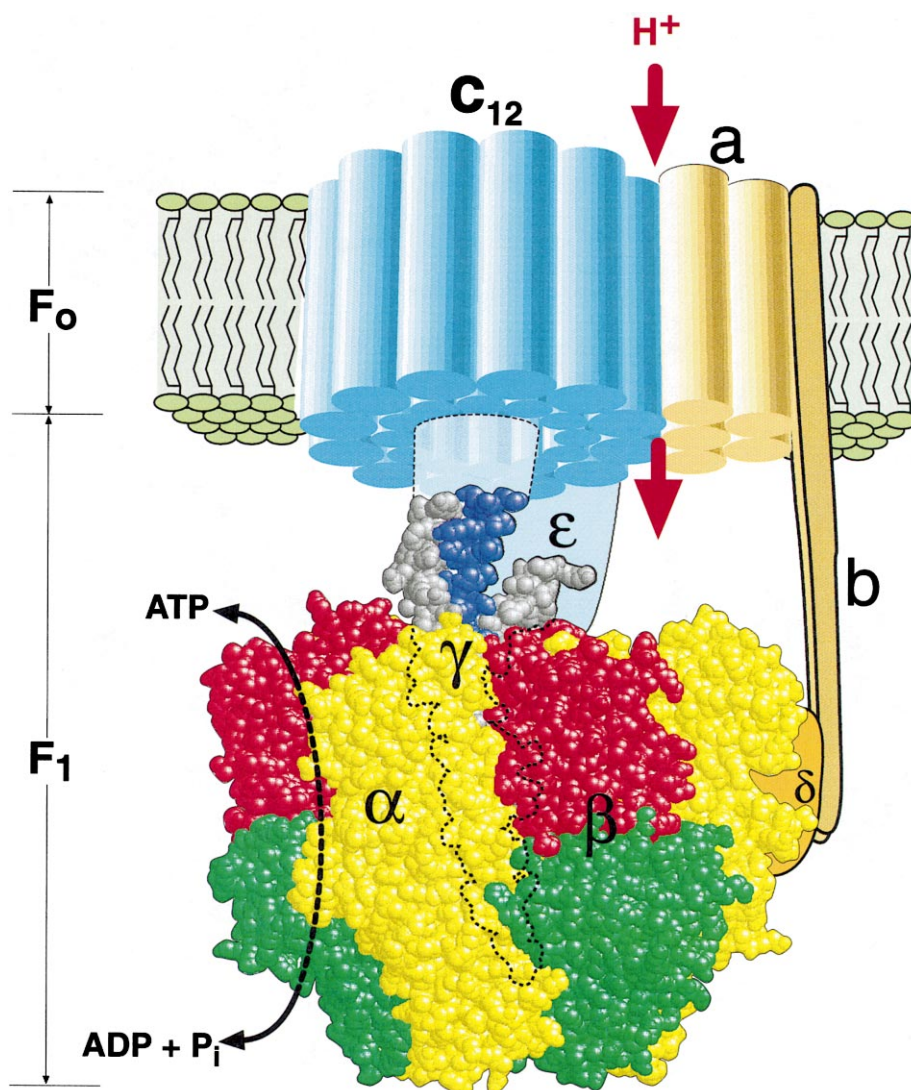


Fig. 1. The geometry of ATP synthase. The soluble F_1 portion lies below the level of the membrane; F_0 is the transmembrane sector. The 'rotor' consists of subunits $\gamma\epsilon c_{12}$, and the 'stator' of subunits $a_b\delta\alpha_3\beta_3$. The F_1 motor experiments were carried out with only $\alpha_3\beta_3\gamma$. (Reprinted from *Structure*, 1999 with kind permission from Elsevier Science Ltd.)

equation must be coupled to the evolution of the chemical state, s , which we can write symbolically as

$$\frac{ds}{dt} = \mathbf{K}(\theta) \cdot s \quad (2)$$

where $\mathbf{K}(\theta)$ is a matrix of all of the rate constants, each of which depends on the angular position of the γ shaft. Our task is to flesh out the specifics of Eqs. 1 and 2. To do this we must construct a model for how the torque, $\tau_H(\theta, s)$ is generated by the hydrolysis cycle, and how the reaction rates, $\mathbf{K}(\theta)$, are coordi-

nated with the rotation so as to achieve the observed rotation rates and mechanical efficiency. We begin by examining the conformational motions of F_1 during the hydrolysis cycle in detail.

2.1. Kinematics: the molecular motions that accompany rotation

The structures elucidated by Walker's laboratory revealed the conformational changes in F_1 that accompanied rotation [8]. They were able to capture the conformations corresponding to three states in

the hydrolysis cycle. We combined the Protein Data Bank (PDB) structures with Boyer's binding change mechanism [9] to construct a movie of the conformational cycle of F_1 .¹ To do this we assumed that the transition between adjacent states shown in the PDB structure corresponded to one third of a rotation by the γ shaft. We then devised a cylindrical interpolation scheme to estimate the conformational sequence through an entire rotation. This gave us the kinematic sequence shown in Fig. 2, from which we deduced the following facts:

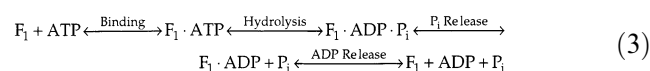
- The major conformational change of the β subunits is a rotation of the upper portion of β in Fig. 2 about 30° with respect to the lower portion. This comes about because of a combination of rotation and shear between helices B and C [10] abutting the catalytic site. We modeled the bending of the β subunits by a relative rotation of the upper and lower portions at an equivalent 'hinge' point located such that it achieves the same motion as the rotation and shear motions in the actual bending motion of β .
- The α subunits alter their conformation only slightly, and passively in response to the β motions.
- The rotation of the eccentric γ shaft is driven by the successive bending of the three β subunits. This bending pushes the region on β near β Ile390 and β Leu391 against γ at the level near γ Met25 and γ Ala235, much like turning the crankshaft on an automobile (Fig. 3).
- The direction of rotation is determined by the relative angular position of the 'most eccentric point' near γ Met25 shown in Figs. 2 and 3 with respect to **Gate 1** near γ Gln255 which we will discuss below.

2.2. Dynamics: the forces that drive rotation

Having established that the bending of the β subunits turns the γ shaft by pushing on its off-axis eccentric portion, we must next determine how the catalytic site generates the forces that drive this bending. In this we are seriously constrained by the

F_1 motor's ability to convert nearly 100% of the free energy derived from the hydrolysis cycle into rotary motion. In Appendix A we show that *the torque generated at the catalytic site must be nearly constant*, which precludes a 'Brownian ratchet' mechanism [1,11,12].

A second constraint arises from the free energy changes during the hydrolysis cycle computed from measurements of the unisite reaction rates (i.e. when nucleotide concentrations are so low that, on average, only one catalytic site is occupied). The overall reactions during the hydrolysis cycle at a catalytic site can be written:²



The unisite free energy diagram in Fig. 4b shows that two major free energy drops take place during this cycle. The first takes place when ATP binds the catalytic site and the second when phosphate is released after hydrolysis [13,14]. This suggests that *the F_1 motor executes two power strokes during each hydrolysis cycle*. We denote these as the primary power stroke (**PS1**) and the secondary power stroke (**PS2**); **PS1** is somewhat larger than **PS2**. Here we present one mechanism of energy conversion that fits these requirements, and that will enable the model to reproduce all of the experimental observations.

In the original formulation of the F_1 motor [2], we assumed that the binding of nucleotide to the catalytic site is converted into elastic strain energy within the β subunit. That is, about $24 k_B T$ is conferred on the protein when ATP binds to the catalytic sites. This phenomenological assumption was sufficient to reproduce the experimental data. Here we present a more detailed scheme which justifies the phenomenological model, and delves somewhat deeper into the events taking place at the catalytic site.

ATP binding involves the formation of hydrogen bonds as the nucleotide thermally settles into the catalytic site, as shown schematically in Fig. 4a. One way to generate a constant force is if the binding process proceeds as a *sequential* annealing of hydrogen bonds, represented by the staircase energy function Fig. 4b. We will call this process the '*Binding*'

¹ Movies of the kinematic motions can be downloaded from: <http://nature.berkeley.edu/~hongwang/ATP-synthase>

² ATP always refers to $Mg^{++} \cdot \text{ATP}$.

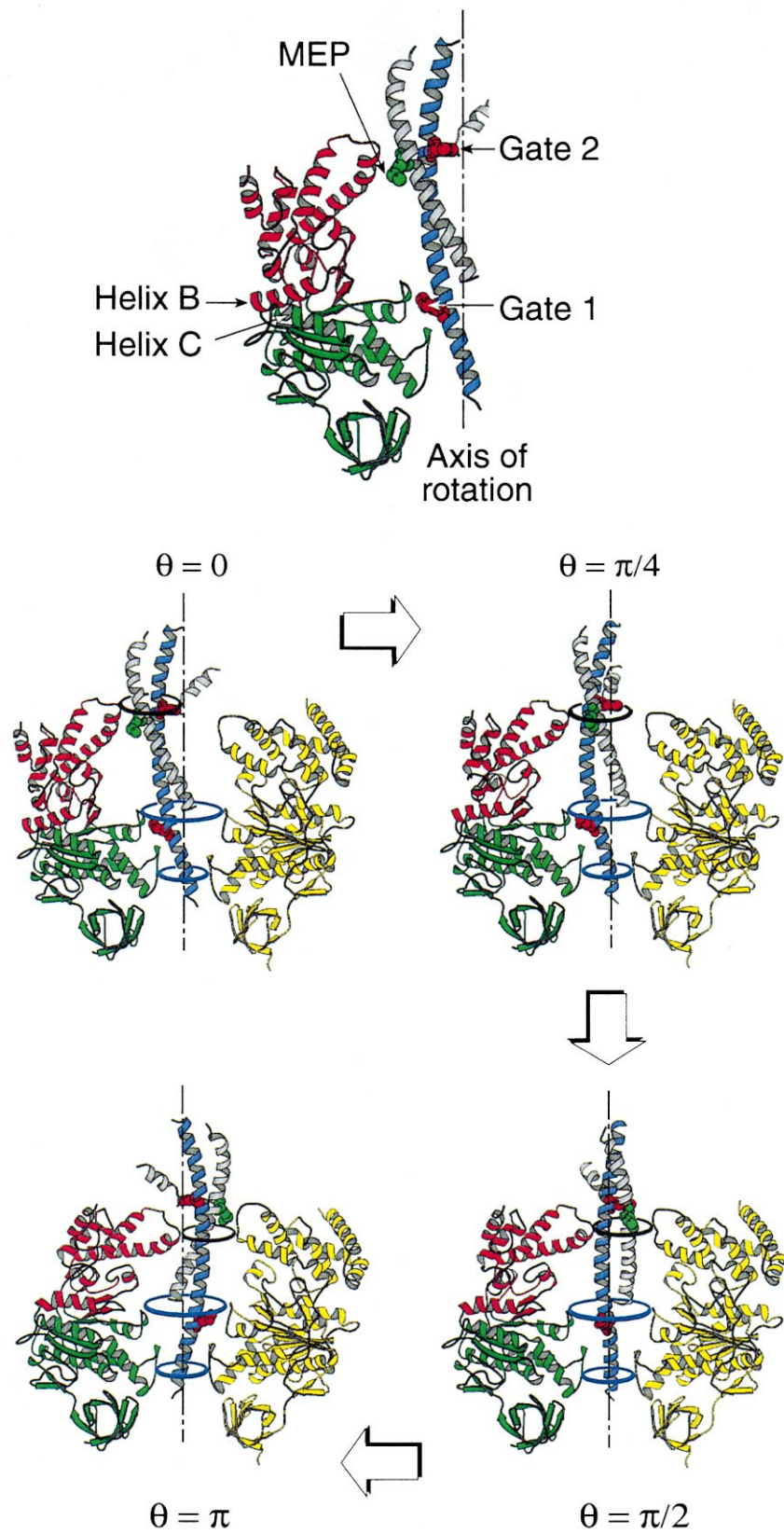


Fig. 2. Conformational changes accompanying the rotation of the γ shaft. The top panel shows the ribbon structure of a β and γ subunit [8]. The top portion of β (red) contains helix B and the bottom portion contains helix C, both of which abut the catalytic site. On the γ coiled coil the ‘most eccentric point’ (MEP, green) is located furthest from the axis of rotation. **Gate 1** and **Gate 2** (red) are located diametrically opposite one another. The bottom four panels show four frames from the intercalation movie. The γ shaft has three contact levels with the $\alpha_3\beta_3$ hexamer. The γ shaft is held at two lower levels (circles at the middle and the bottom) by the $\alpha_3\beta_3$ hexamer. The top portion of β impinges on γ at the level near the MEP (the circle at the top). The stop frames at $\theta=0, \pi/4, \pi/2,$ and π show that the ‘bearing’ level regions (the middle and bottom circles) remain coaxial, while the driving level contact (top circle) rotates off-center in concert with the bending of the β s.

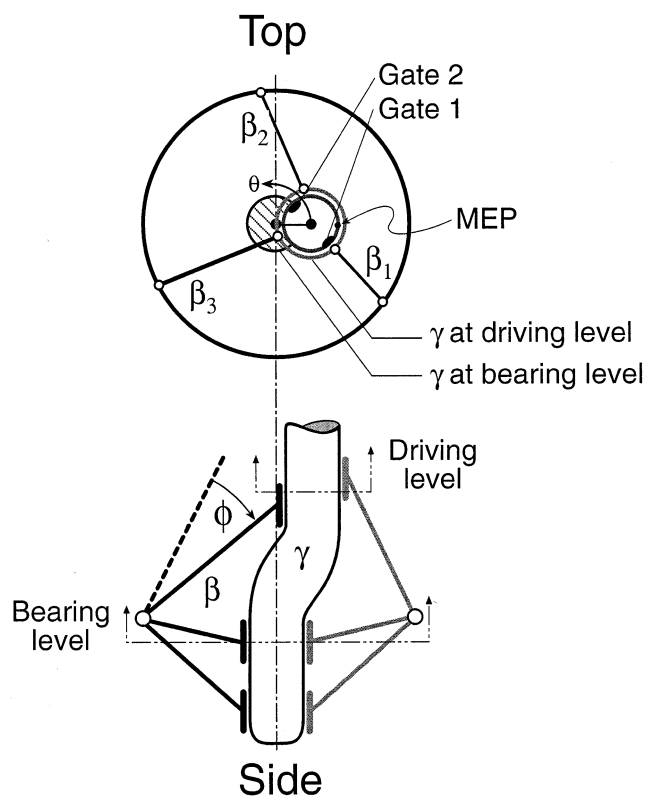
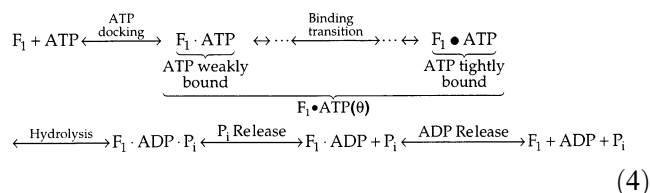


Fig. 3. Schematic of the mechanical escapement. Here we abstract the structure in Fig. 2 as a cartoon frame. The γ shaft is held by $\alpha_3\beta_3$ at the middle and the bottom levels. At the top level (the driving level), the γ shaft is off-center. As the β s bend, they generate a rotary torque by pushing off-axis on the γ shaft at the driving level. When projected onto the driving level and viewed from the top, the ‘most eccentric point’ (MEP) leads **Gate 1** in the counter-clockwise direction. Thus when the interaction of **Gate 1** with β admits ATP to the catalytic site and starts the bending motion of a β , the MEP has passed that β . Thus the bending motion of β drives the γ shaft to rotate in the counter-clockwise direction.

Zipper’; Appendix B discusses this notion in more detail. There we show that this mechanism has the required high energy conversion efficiency, and that it generates a force that is approximately constant with displacement (similar to surface tension or a pre-stretched spring), as compared to a force that increases with displacement characteristic of an elastic spring. Moreover, when the cycle is reversed during ATP synthesis, the Binding Zipper mechanism provides an efficient mechanism to ‘unzip’, that is, gradually reduce the binding affinity of ATP and release it with a minimum of dissipation. Thus we enlarge the reaction sequence in Eq. 3 to the following kinetic scheme:

ASSUMPTION: *The Binding Zipper*



Here the large dot is intended to distinguish the tight binding state at the end of the Binding Zipper from the weak binding state when ATP first enters the catalytic site. Eq. 4 decomposes the binding step in Eq. 3 into ATP docking followed by a sequence of substeps corresponding to the zipping of bonds between ATP and the catalytic site. Because of the tight mechanical escapement, as the binding transition ad-

vances, the β subunit bends, and the γ subunit rotates. In the model we shall separate the kinetic transitions in equation into two categories: (i) kinetic transitions associated with changes in the *occupancy* of the catalytic site, and (ii) kinetic transitions associated with *rotation* of the γ shaft. The kinetic states, s , in Eqs. 2 and 3 describe only the *occupancy* of the catalytic site. The rotation of γ is described by Eq. 1.

In order to release the hydrolysis energy in two steps we make the following

ASSUMPTION: *The open configuration is the rest position of β when it is empty. As the binding free energy of ATP generates a constant force to bend β (the Bind-*

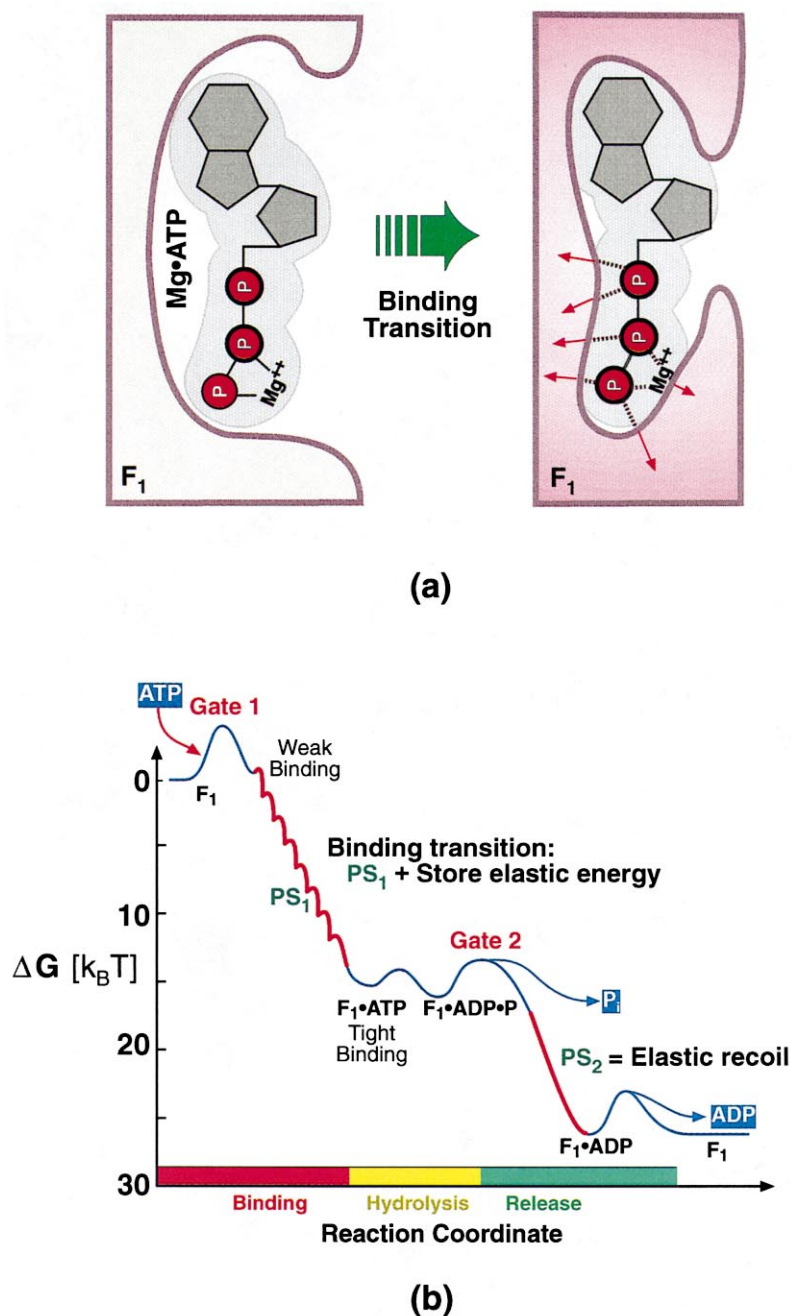
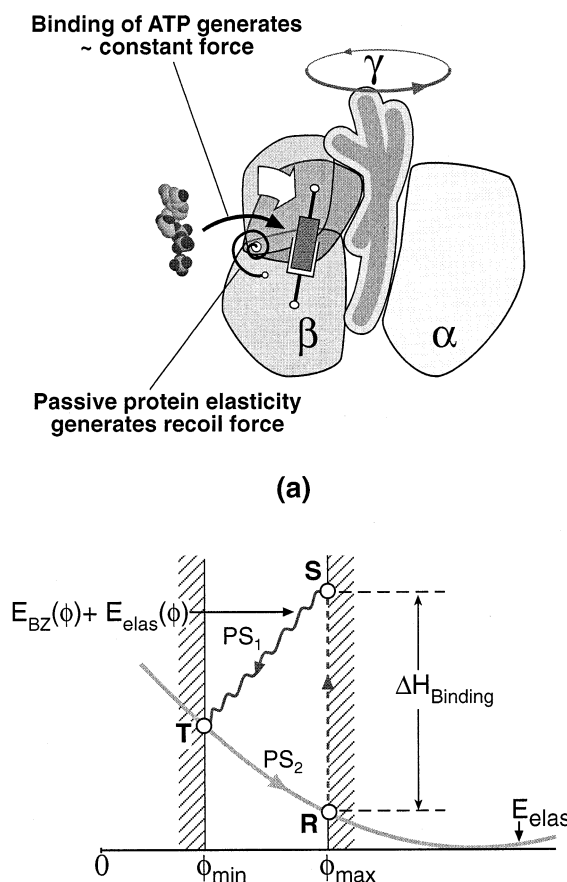


Fig. 4. Modeling the power stroke. (a) The Binding Zipper: ATP binds to the catalytic site by a rapid thermal ‘zippering’ of hydrogen bonds. The closing of the site around the nucleotide creates an approximately constant torque about the hinge point in β , causing the upper portion of β to rotate with respect to the lower portion. At the end of the power stroke ATP is tightly bound. The energy in the γ phosphate bond is used to break the tight binding so that phosphate and ADP can be released. (b) Free energy diagram for the hydrolysis cycle: The free energy levels are calculated from the reaction rates measured at unisite reaction conditions [13]. In the calculation, we used [ATP]=1 mM; [ADP]=0.01 mM and [P_i]=0.1 mM. The two major free energy drops occur at nucleotide binding and upon phosphate release. The second drop reflects release of elastic strain energy stored in β during nucleotide binding. There are two power strokes: the primary power stroke (PS1) is driven by the Binding Zipper, and the secondary powerstroke (PS2) is driven by the elastic recoil of the passive spring. The magnitudes of the free energy drops are accurate, but the sizes of the energy barriers are not to scale. Note that the ‘states’ F₁•ATP and F₁•ADP correspond to a range of free energies since the chemistry is coupled to the bending of the β subunits. ‘Gate 1’ controls the admission of ATP to the catalytic site and ‘Gate 2’ controls the release of phosphate (see Fig. 7).

Fig. 5. Modeling the forces. (a) The mechanical model. The β subunit is divided into an upper and lower portion that can rotate about a hinge point. The elasticity of the protein is represented by the coiled spring at the hinge. Upon ATP docking at the catalytic site, a constant force generator (the Binding Zipper) is introduced that tends to close the angle between the two portions. We measure the bending of the β subunit by the angle ϕ , which is sterically constrained to lie between ϕ_{\min} and ϕ_{\max} . From the kinematic study $\phi_{\max} - \phi_{\min} \approx 30^\circ$. (b) Internal energy of the β subunit. The internal energy includes both the internal energy of the protein and the energy of interaction between the nucleotide and the catalytic site. The enthalpic part of the assembly free energy results in $\alpha_3\beta_3$ with a resting elastic energy at **R**. Immediately upon entering the catalytic site ATP initiates the Binding Zipper and shifts the internal energy upwards to state **S** (dashed line) by an amount equal to the enthalpic part of the binding free energy. The binding transition from weak to tight generates the primary power stroke (**PS1**) from **S** to **T**, which closes the angle ϕ between the upper and lower portions of β . This binding transition also stores elastic energy in the protein when β is bent against its elasticity. Upon release of phosphate, the overcompression of the passive spring drives the secondary power stroke (**PS2**) by elastic recoil from **T** to **R**.



R → **S**: ATP docking initiates the Binding Zipper
S → **T**: Binding transition = **PS1** + Store elastic energy
T → **R**: Elastic recoil = **PS2**

(b)

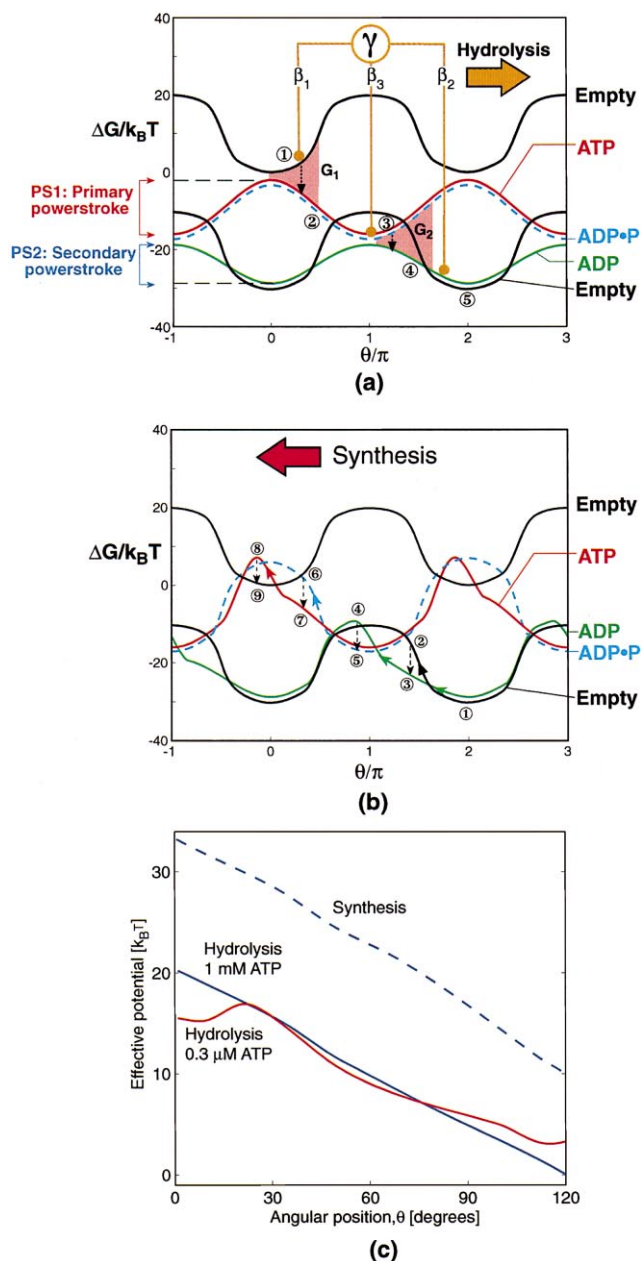
ing Zipper), a portion of the force is used to store energy in β as elastic strain.

This means that the free energy induced by ATP binding acts in two ways: (i) directly to bend β and turn the γ shaft (**PS1**), and (ii) to store elastic energy in the β subunit as it bends against its elastic resistance. The second power stroke (**PS2**) is driven by the recoil of this stored elastic energy. To model this, we treat the β subunit as an elastic body, as shown schematically in Fig. 5a. The free energy associated with assembly of the protein generates a 'resting state strain' when the catalytic site is unoccupied.³ The passive elasticity of the β subunit is represented by a spring at the hinge axis. The constant force generated by the ATP Binding Zipper is represented symbolically by an active element that is introduced at the moment of ATP docking. Fig. 5b shows the energy changes *within* the protein, in contrast to the *externally* measured free energy changes in Fig. 4b.

³ The structure of nucleotide free $\alpha\beta$ suggests that the open (unbent) configuration is a stable rest state for an empty β [18]. That is, this stable configuration is a constrained elastic energy minimum created during assembly by the free energy of association. If so, then when β bends, additional elastic strain energy is stored in the protein.

As ATP settles into the catalytic site, the binding free energy drives the primary power stroke (**PS1**) that turns γ by about a third of a revolution. At the same time, it compresses the passive spring, storing elastic energy. When phosphate is released, this stored elastic energy drives the secondary power stroke (**PS2**) as it recoils from its strained state. This recoil power stroke assists the next β subunit in the hydrolysis sequence as it executes its primary power stroke. We will see later how these two power strokes are coordinated with the hydrolysis reactions. Releasing the energy resulting from ATP binding in two steps helps making the output torque uniform and increases the mechanical stability of the F_1 motor because the drive force on the γ shaft comes from two of the three β s at any moment. Therefore, during

Fig. 6. The elastic potentials associated with the F_1 motor. (a) The potentials that drive the F_1 motor. The interaction between the γ shaft and each catalytic site is described by a set of four potentials which vary as functions of θ . Each potential curve represents the free energy of one β subunit and the nucleotides in solution. The potentials shown here are for the concentrations: $[ATP] = 1$ mM; $[ADP] = 1$ μ M; $[P_i] = 1$ μ M. This set of unphysiological concentrations is selected to make the four potentials well separated from each other. The vertical distance between the two **Empty** curves shown corresponds to the free energy change of the system after one hydrolysis cycle. The total interaction between the γ shaft and the three β s is described by three sets of these potentials offset by $2\pi/3$. Here we visualize the total interaction by placing three legs, rigidly connected and offset by $2\pi/3$, on one set of potentials, so that each leg is on the potential curve corresponding to the reaction state of a β . The interaction between the potentials and the leg marked β_1 represents the interaction between β_1 and the γ shaft. A typical sequence for β_1 is shown beginning on the top **Empty** state curve and ending on an **Empty** state curve ΔG_{ATP} lower after completion of one hydrolysis cycle. (1) **Gate 1** admits ATP to the catalytic site of β_1 . (2) the primary power stroke of β_1 drives γ , assisted by the secondary (recoil) power stroke of β_3 . (3) **Gate 2** triggers the release of phosphate on β_1 . (4) The secondary (recoil) power stroke of β_1 assists the primary power stroke of β_2 . (5) ADP dissociates returning the site to the empty state. (b) The potentials that synthesize ATP. The F_0 motor supplies torque to rotate the γ shaft in the direction opposite to that in (a). In order to synthesize efficiently, additional ‘bumps’ must be added to the **ADP** potential to retard rotation until phosphate binds, and to the **ATP** potential to ensure release of ATP as γ turns. We ascribe one or both of these bumps to the interaction between the γ subunit and the DEL-SEED regions of the β s. The presence of these bumps do not appreciably affect the motor performance. The sequence of steps (1) \rightarrow (9) traces a typical pathway wherein the rotation of γ activates ADP and phosphate binding to the catalytic site and subsequent release of ATP. (c) The effective driving potential seen by γ . The effective potentials for hydrolysis and synthesis were computed by averaging the torques in the 64 chemical states and integrating to build the average potential seen by γ . The dashed line is the effective potential from F_1 seen by the F_0 motor when it generates 46 pN \cdot nm of torque and synthesizes 210 ATP/s at concentrations: $[ATP] = 0.2$ mM; $[ADP] = 0.1$ mM and $[P_i] = 2$ mM. The load torque is nearly constant. The solid lines are the effective potentials generated by F_1 under high ATP concentration ($[ATP] = 1$ mM; $[ADP] = 0.01$ mM and $[P_i] = 1$ mM) and low ATP concentration ($[ATP] = 0.3$ μ M; $[ADP] = 0.1$ μ M and $[P_i] = 0.1$ μ M). The slopes (i.e. the torques) of both hydrolysis potentials are ~ 40 pN \cdot nm, which is the same value computed by Kinosita et al. from their experimental data [51]. At low ATP concentration, the activation energy barrier on the effective potential curve near $\theta = 20^\circ$ represents the entropic barrier required for an ATP to diffuse to and enter the catalytic site.



the rotation, the stress is more uniformly distributed on the $\alpha_3\beta_3$ barrel.

Both power strokes, **PS1** (the Binding Zipper) and **PS2** (the elastic recoil), can be expressed in terms of a potential function that depends on the bending angle, ϕ , of the β subunit. However, equation governing the rotation of the γ shaft is in terms of the rotation angle θ . Because of the high energy conversion efficiency the mechanical coupling between the

bending of β and the turning of γ must be very tight. Therefore, there must be a unique relationship between the bending angle, ϕ , and the rotation angle, θ , which we can deduce via trigonometry [2]. Using this relationship we can express the torque in equation in terms of an elastic potential that depends only on the rotation angle, θ , and the chemical state, s : $\tau(\theta, s) = -\partial V(\theta, s)/\partial \theta$.

For each catalytic site there will be four potentials, each corresponding to a kinetic state s in the hydrolysis Eq. 3. To compute these potentials explicitly we need the passive elastic constant and the free energy of the Binding Zipper. The former can be estimated from the measured unisite free energy drop associated with the phosphate release, and the latter is computed from the sum of the two free energy drops in the unisite reaction (because the Binding Zipper is responsible for both driving **PS1** and storing the elastic energy for **PS2**, see Appendix B). These potentials are drawn in Fig. 6a for the F_1 motor consisting of only $\alpha_3\beta_3\gamma$. We visualize the three β s driving the rotation of γ by connecting three ‘legs’ spaced $2\pi/3$ apart, so that each leg rests on the potential corresponding to the hydrolysis state of that catalytic site. Note that the potentials are computed from the mechanical model for force generation: the Binding Zipper generates the primary power stroke, and the angle spring generates the recoil secondary power stroke. Thus the shapes of the potentials are independent of the concentrations of reactants and products. The *vertical spacings* between the potentials depend on the entropic contributions to the free energy, which affect the transitions between the potentials. The solution ATP concentration controls the ATP binding rate, i.e. the transition from the **Empty** potential curve to the **ATP** curve. The concentrations of ADP and P_i control the rates ADP and P_i rebind to the catalytic site.

There is an additional crucial point associated with the Binding Zipper mechanism for force generation. At the completion of the power stroke ATP is bound tightly to the catalytic site. How then is the site to release the hydrolysis products to permit the next hydrolysis cycle to commence? In Appendix B we argue that the enthalpic component of the hydrolysis free energy is sufficient to reduce the binding affinity of ADP and P_i sufficiently for them to dissociate from the catalytic site. Next we must compute how

the system switches between these four potentials as the hydrolysis cycle proceeds.

2.3. Coordinating the mechanical and chemical cycles

The 4-step hydrolysis reaction given in Eq. 3 proceeds at each catalytic site, so there are $4^3 = 64$ possible chemical states. (*Remember*: Eq. 3 describes only the change in occupancy of a catalytic site; the binding transition associated with the rotation of γ is modeled by equation 1.) One can visualize the reaction state, s , as a point hopping along a $4 \times 4 \times 4$ cube.⁴ Since the kinetic equations are stochastic, the point s wanders statistically through the reaction cube, its trajectory governed by Eq. 2. However, in order to achieve the required efficiency the reactions on the three catalytic sites can not proceed independently, but must be coordinated with the rotation of γ . Thus the path of s is not totally random, but tends to follow a preferred set of pathways in the reaction cube (which is why the matrix of rate constants, $\mathbf{K}(\theta)$, in Eq. 2 are functions of θ). But how is this coordination accomplished?

One candidate mechanism was discovered by Nakamoto’s lab, who identified two regions on γ located diametrically opposite one another on the γ shaft, as shown in Figs. 2 and 3. These regions interacted sterically and/or electrostatically with regions on β that in turn were conformationally linked to the catalytic sites [19,20]. We shall adopt these candidates as the ‘camshaft and distributor cap’ that synchronizes rotation of γ with the catalytic cycle:

ASSUMPTION: *There are two ‘gating’ regions on γ which interact with the β subunits. **Gate 1** ($G1 = \gamma\text{Gln255}$) controls the admission of ATP to the catalytic site. **Gate 2** ($G2 = \gamma\text{Arg228}$) interacts with the $\beta\text{DELSEED}$ region, and controls the release of phosphate after hydrolysis.*

The coupling between the rotation of γ and the chemical reaction on β s is coordinated by the two gates, as shown in Fig. 7. At the beginning of a power stroke, in the upper left panel, the P_i release on β_3 is coordinated by **Gate 2**, and the ATP binding

⁴ Since the hydrolysis cycle is periodic, this is actually a 3-dimensional torus: when s emerges from one face it recycles back through the opposite face.

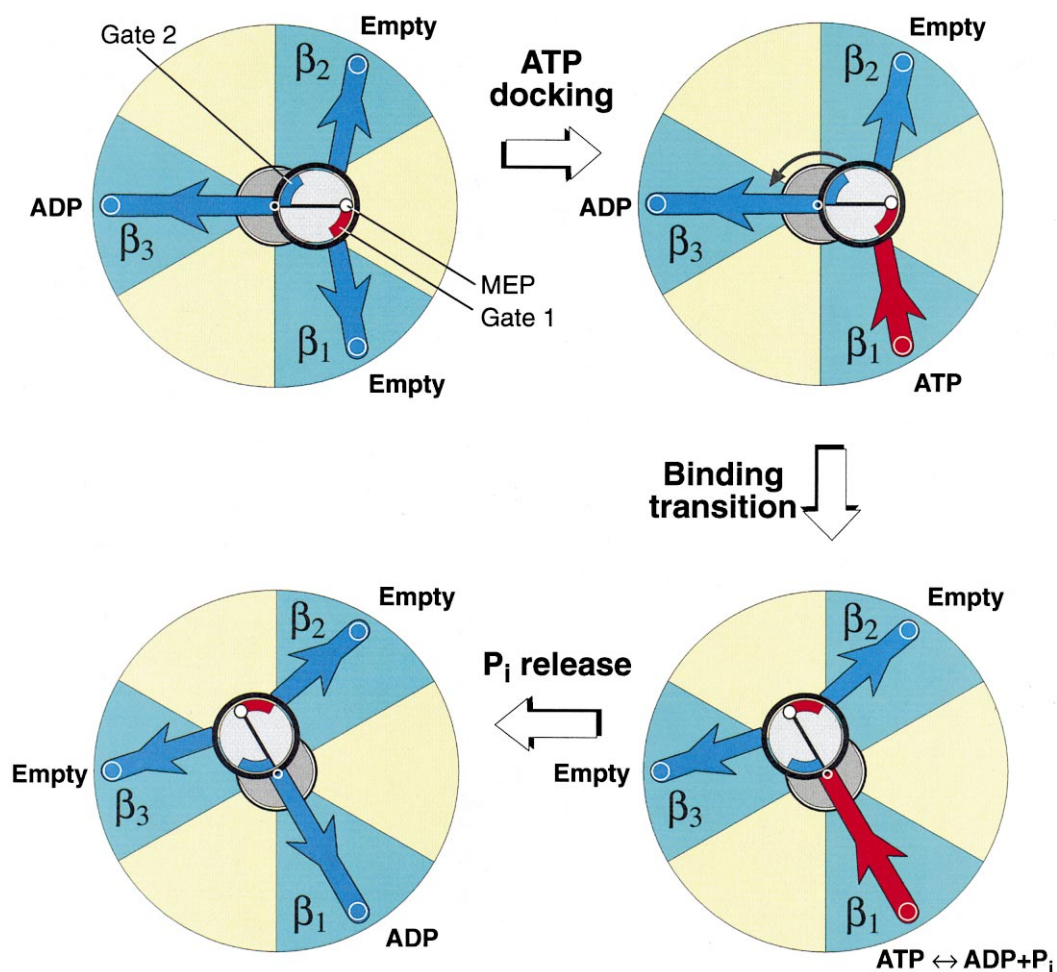


Fig. 7. Coordinating the chemistry with the mechanics. The sequence of events associated with a rotation of $2\pi/3$ at low ATP concentration. The diagram shows a schematic top view of the $\alpha_3\beta_3\gamma$ hexamer as in the top panel of Fig. 3. The heavy circle is a cross-section of the γ shaft at the driving level showing the location of the most eccentric point (MEP), and the regions on γ corresponding to **Gate 1** (γ Gln255), that controls the admission of ATP to the catalytic site, and **Gate 2** (γ Arg228) that controls the release of phosphate from the catalytic site. This sequence is extracted from an animation movie of the cycle that can be viewed at the website in footnote 1. Frame 1: The catalytic sites on β_1 , β_2 , and β_3 are in states **Empty**, **Empty** and **ADP**, respectively. However since β_1 is interacting with **Gate 1**, it is much more likely for an ATP to enter the catalytic site of β_1 (rather than the catalytic site of β_2) and initiate the primary power stroke of β_1 (**PS1** in Fig. 4b). β_3 is interacting with **Gate 2**, which triggers P_i release and starts the recoil power stroke on β_3 (**PS2** in Fig. 4b). Frame 2: After ATP enters the catalytic site of β_1 , the binding transition from weak to tight generates a constant force to bend β_1 . Viewed from the top, β_1 pushes at the off-center level of the asymmetric γ shaft while β_3 pulls. The direction of rotation is determined by the relative angular position of **Gate 1** and the MEP. Frame 3: β_1 has reached the end of the primary power stroke when the MEP is at 'top dead center' with respect to β_1 's power stroke direction. At this point, the binding transition from weak to tight has completed and ATP is in equilibrium with ADP and P_i in the catalytic site. Frame 4: Interaction of β_1 with **Gate 2** has released P_i initiating the secondary power stroke of β_1 . Viewed from the top, this appears as a 'pull' on the γ shaft. The secondary power stroke of β_1 will coordinate with the primary (pushing) power stroke of β_2 when **Gate 1** admits an ATP to the catalytic site of β_2 .

on β_1 (rather than on β_2) is promoted by **Gate 1**. After a rotation of $2\pi/3$, in the lower left panel, the P_i release on β_1 is coordinated by **Gate 2**, and the ATP binding on β_2 (rather than on β_3) is promoted by **Gate 1**.

This is not the only possible mechanism for coordinating the hydrolysis cycle with rotation of γ . Sequential admission of ATP to each catalytic site can be coordinated without **Gate 1**. As γ rotates, the top portions of the β subunits not only bend but also

rotate in the plane perpendicular to the γ shaft. In the upper left panel of Fig. 7, the top part of β_1 is twisted with respect to its bottom part in the clockwise direction while the top part of β_2 is twisted in the counter-clockwise direction. Although both β_1 and β_2 are empty (upper left panel of Fig. 7), this difference in the orientation of the top part with respect to the bottom part could lower the activation energy significantly for ATP binding on β_1 . Thus ATP is much more likely to bind to the β immediately behind the most eccentric point (β_1 in the upper left panel and β_2 in the lower left panel of Fig. 7) and the F_1 motor rotates in the counter-clockwise direction.

There is a third possibility for coordinating the hydrolysis cycles that does not involve rotation of γ . The catalytic sites are located at β - α interfaces, with most of the important residues on β , but a few important ones on α (e.g. $\alpha R376$) [8,14]. Binding of ATP to a catalytic site creates an asymmetric motion that generates not only the bending of β , but also a small rotational ‘propeller’ motion in the direction of rotation as well. This asymmetrical motion could preferentially signal the next catalytic site 120° ahead in the rotational scheme by shifting slightly the position of $\alpha R376$. Thus the orientation of β , either alone or in conjunction with the angular position of the asymmetric γ shaft, could trigger the admission of ATP to the next catalytic site. The amount of strain energy involved would be minimal if nucleotide binding were entropically controlled, perhaps by the P-loop over the catalytic site. Alternatively, control could be exercised by a small motion of the few residues on the α subunit that participate in catalysis [14]. The possibility of intersite signaling via α rather than γ also has been suggested by [10]. Since we have no information on the relative contribution of conformational coupling via α we can only mention it as a theoretical possibility.

All these different coordination mechanisms use the angular position of γ with respect to a β subunit to control the reaction on that β . In the mathematical model, they are similar to each other, and any one could be easily incorporated into the model if evidence warrants.

2.4. Computing the multisite reaction rates

The F_1 motor operates under ‘multisite’ conditions when more than one catalytic site is occupied. Unfortunately, accurate kinetic measurements have been made only for unisite condition, when the ATP concentration is so low that, on average, only one site is occupied (the free energy curve in Fig. 4 is constructed from unisite kinetic data). Therefore, to construct the multisite kinetic rates we must make estimates about how the kinetics scales. For example, the rate of P_i release from a catalytic site depends on the rotational position of γ and on the occupancy of the other two sites. We build this multisite rate, k^{Multi} , from the measured unisite rate, k^{Uni} according to the following

ASSUMPTION: *The multisite rates can be constructed by multiplying the unisite rates by functions that account for (i) multisite occupancy, (ii) angular control of ATP binding and phosphate release by Gate 1 and Gate 2, and (iii) the effect of differences in elastic energy between the current position and the rest position. For example, the forward reaction rates are computed as:*

$$\frac{k_f^{\text{Multi}}(\theta, \beta_{i-1}, \beta_{i+1})}{\text{Multisite forward rates}} = \frac{k_f^{\text{Uni}}}{\text{Unisite forward rates}} \cdot \frac{f_{\text{Occ}}(\beta_{i-1}, \beta_{i+1})}{\text{Effect of occupancy of adjacent sites}} \cdot \frac{g_{\text{Gate}}(\theta)}{\text{Effect of Gates}} \cdot \frac{\exp\left(\frac{\lambda \cdot \Delta E(\theta)}{k_B T}\right)}{\text{Effect of elastic energy difference}} \quad (5)$$

We used the unisite data of Weber and Senior [13]; the details of how all the reaction rates were estimated are given in [2]. Although sensible, there are some uncertainties in this factoring. However, when better kinetic data are available it will be easy to incorporate into the model.

2.5. Putting it all together: the hydrolysis motor and the synthesis machine

We now have in hand the ingredients required by the model Eqs. 1 and 2. All of the parameters are taken directly, or estimated from, experimental data. The computed solutions reproduce many of the empirical measurements, from the qualitative appearance of the stochastic trajectories – including their occasional reversals – to the quantitative fit of the load velocity measurements by Yoshida’s and Kinoshita’s groups [2]. Some of these results are shown in Fig. 8; others can be found in [2]. Of course, the

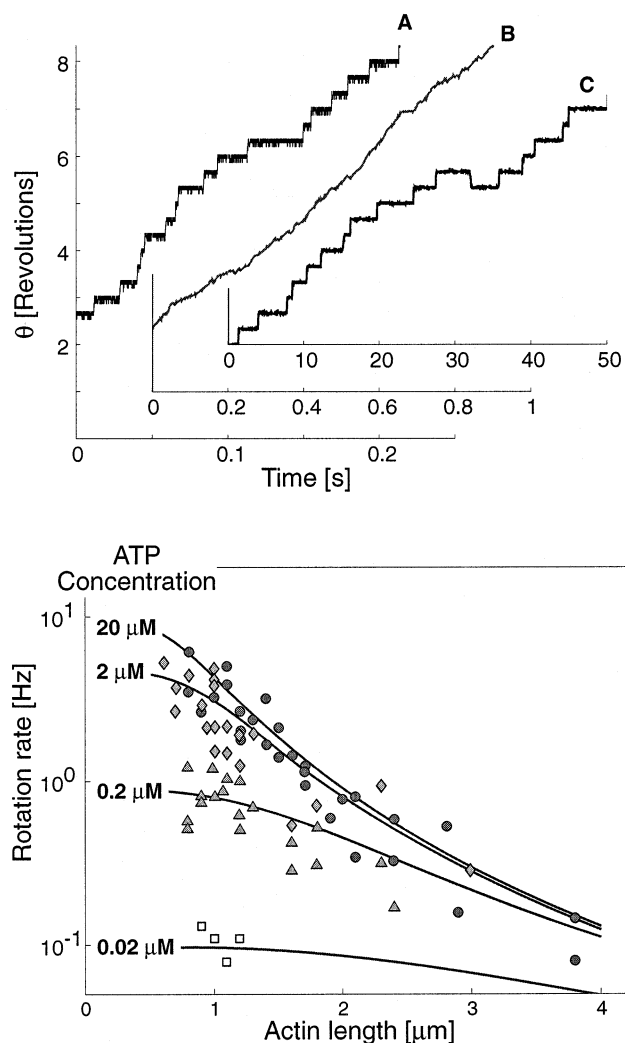


Fig. 8. Fitting the model to experiments. (a) Trajectories. The rotor advances stochastically showing the observed stepwise behavior at low ATP concentration (trajectory C: $[\text{ATP}] = 20 \text{ nM}$; $[\text{ADP}] = 20 \text{ nM}$ and $[\text{P}_i] = 20 \text{ nM}$) and smooth advance at high ATP concentration (trajectory B: $[\text{ATP}] = 2 \text{ mM}$; $[\text{ADP}] = 0.02 \text{ mM}$ and $[\text{P}_i] = 0.5 \text{ mM}$). Trajectory A is computed for the same concentrations as trajectory B but with low viscous load corresponding to no actin filament. (b) Load velocity behavior. The model (solid lines) fits the (viscous) load velocity behavior over a wide range of ATP concentrations (data from [6]). For the simulations shown in this panel, we take $[\text{ADP}] = [\text{P}_i] = [\text{ATP}]$ so only ATP concentrations are shown.

model is surely not correct in all its aspects. However, it does provide a conceptual and computational framework within which new theoretical and experimental investigations can be posed.

The most striking result of this analysis is that a

protein machine can convert chemical energy to mechanical motion with an efficiency that approaches 100%, far higher than any other protein motor, and better than most man-made mechanochemical devices. The efficiency of F_1 's mechanochemical cycle arises from several design features that arose and were fine tuned during their long evolutionary history.

- Mechanical dissipation is minimal because the bending of β is tightly coupled mechanically to the rotation of γ (i.e. there are no 'rattles'), and the hydrophobic sleeve holding the γ shaft is nearly frictionless.
- During hydrolysis, the Binding Zipper utilizes the binding free energy of ATP to generate a nearly constant primary power stroke. At the end of the power stroke, the ATP is tightly bound; the energy in the γ phosphate bond is used to break the weakened binding so that ADP and phosphate can be released (see Appendix B).
- The β subunit can store elastic strain energy during the primary power stroke to be released later during the secondary power stroke.
- **Gate 1** and **Gate 2** coordinate the mechanical and chemical cycles so that ATP is admitted to the catalytic site and phosphate released at the appropriate rotational angle.
- During synthesis, the sequential 'unzipping' of the bonds between the newly formed ATP and the catalytic site is also nearly lossless, since there are no significant elastic recoils.⁵

A crucial test of the model is whether it can, when driven backwards, synthesize ATP. To do this, torque must be supplied to F_1 in an amount equivalent to that produced by the F_0 motor. As we will see below, the F_0 motor generates a torque in 12 equal stochastic steps per revolution, with the average passage of four protons per ATP released from F_1 .

⁵ Some authors have hypothesized that the turning of F_0 builds up elastic strain in F_1 until a threshold is reached where upon the catalytic site pops open and releases ATP [15–17]. However, this would be very inefficient since all of the elastic energy stored would be dissipated as heat. The Binding Zipper suffers only small elastic recoils as each bond breaks. This is discussed more fully in Appendix B.

Moreover, because of the elastic coupling between the rotor and stator (Fig. 9a), the torque seen by F_1 is nearly constant. Fig. 9b shows that when the F_1 synthesizer is coupled to the F_0 motor which is driven by a proton motive force of 220 mV (the physiological proton motive force in mitochondria), it can indeed produce ATP at the observed rate. However, in order to do this the model must be modified in a particular way.

Fig. 6b shows the elastic potentials for synthesis. Comparing them with Fig. 6a, synthesis requires a bump on the ADP potential to hold up rotation of γ until P_i binds. Is this an ad hoc addition? The experiments on the F_1 motor were carried out in the absence of the ϵ subunit, which forms part of the shaft, along with the γ subunit, and which interacts with the DELSEED region on β . The presence of the ϵ subunit is necessary to interact with the DELSEED region on β to hold up the rotation of γ until phosphate binds. Interestingly, the F_1 motor turns somewhat slower when the actin filament is attached to the ϵ subunit rather than the γ subunit [21]. This may be due to the additional interaction between the $\delta\epsilon$ and β subunits. Adding these bumps to the F_1 motor potentials in Fig. 6a does not affect the motor performance very much, which accords with the experiments reported in the presence of ϵ [21].

As we will see below, the F_0 motor delivers torque to F_1 in 12 equal stochastic steps. However, in order to maximize the efficiency of ATP synthesis, the Binding Zipper must be reversed so that ATP binding is weakened one hydrogen bond at a time by the torque generated in F_0 . In this way, energy is delivered gradually from F_0 to the catalytic site and is stored in the form of ATP binding free energy before

the ATP dissociates, carrying the binding free energy with it. To accomplish this the coupling between F_0 and F_1 must be elastic; that is, the γ and b subunits must not be rigid. As we discuss in Appendix C, the elastic coupling between F_0 and F_1 is *not* used to store energy from several steps of F_0 and deliver it all at once to the catalytic site. Rather, this elasticity smoothes out the energy transduction by taking the stochastic stepwise torque from F_0 and delivering it smoothly – and thus more efficiently – to the catalytic sites in F_1 permitting the bonds to be broken sequentially and with minimum dissipation.

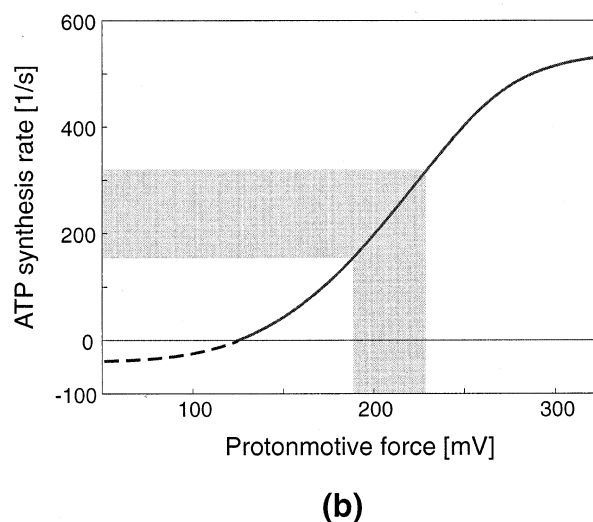
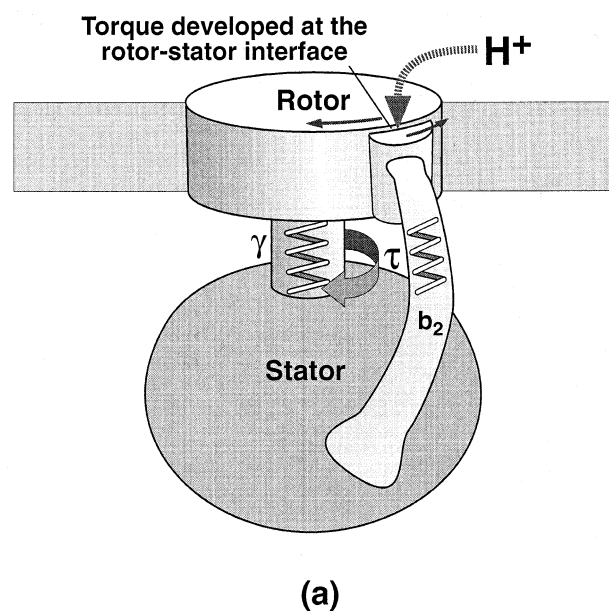


Fig. 9. (a) Elastic coupling between F_0 and F_1 . Because torque is developed at the rotor–stator interface the rotor and stator tend to counter-rotate. The torsional elasticity of γ and the bending and stretching elasticity of b_2 create an elastic coupling between F_0 and F_1 that smoothes out the stochastic progression of the F_0 motor. Thus during synthesis, F_1 sees a nearly constant torque from F_0 . In F_1 this constant torque releases ATP from the catalytic site by unzipping the bonds in a nearly lossless process. (b) When driven by a constant torque generated in the F_0 motor with a proton motive force of 220 mV, the model synthesizes ATP at the correct rate (shaded band). The concentrations are $[ATP]=0.2$ mM, $[ADP]=0.1$ mM and $[P_i]=2$ mM.

Fig. 10. The rotor–stator structure and energetics. (a) Schematic of the rotor–stator assembly in *P. modestum*. The rotor section below the level of the membrane contains the 12 ion binding sites. The stator contains an aqueous channel that conducts ions from the periplasmic (positive) reservoir to the level of the ion binding sites. The positive stator charge, R227, blocks leakage of ions along the polar strip at the right connecting the aqueous channel to the cytoplasm. (b) Face-on view of the rotor–stator assembly. Rotation during ATP synthesis is to the left. Ions from the periplasmic reservoir can access the rotor sites within the aqueous channel, but ions can only exit to the cytoplasm by boarding a rotor site and passing through the dielectric barrier forming the left wall of the channel. If the occupied site moves to the right, it quickly loses its ion back to the channel when it approaches the positive stator charge, R227. (c) Free energy diagram of one rotor site as it passes through the rotor–stator interface. Ion binding and dissociation to the rotor site switch the potentials between that corresponding to an empty site (solid line) and an occupied site (dashed line). 1→2: the rotor site just outside the stator diffuses to the left bringing the empty (negatively charged) site into the attractive field of the positive stator charge (R227) which pulls it into the stator. 2→3: the membrane potential biases the thermal escape of the site to the left by tilting the potential and lowering the left edge. 3→4: the site quickly picks up an ion from the periplasmic channel. This switches the site to the occupied (dashed) potential. 4→5: the occupied rotor site can now pass through the dielectric barrier, driven by diffusion and the pulling of the next rotor site towards the stator charge. If the site diffuses to the right, either the ion dissociates as it approaches the stator charge, or if it diffuses into the interface, it is reflected by the repulsion between the stator charge and the occupied site dipole. 5→6: upon exiting the stator the site quickly loses its ion. Now charged, the site sees the stator dielectric barrier which prevents back diffusion. The cycle decreases the free energy of the system by an amount equal to the electromotive force: $\Delta\mu = \Delta\psi - 2.3(RT/F)\Delta pNa$, where F is the Faraday constant. The free energy changes accompanying ion binding from the periplasm and dissociation to the cytoplasm are ΔG_P and ΔG_C , respectively.

→

3. The F_o motor

The F_o portion of ATP synthase is also a rotary engine, but it draws its energy not from the hydrolysis cycle of ATP, but from the chemical energy stored in a transmembrane proton motive force. At equilibrium, thermodynamics gives equal weight to the concentration and electrical components of the proton motive force (pmf):

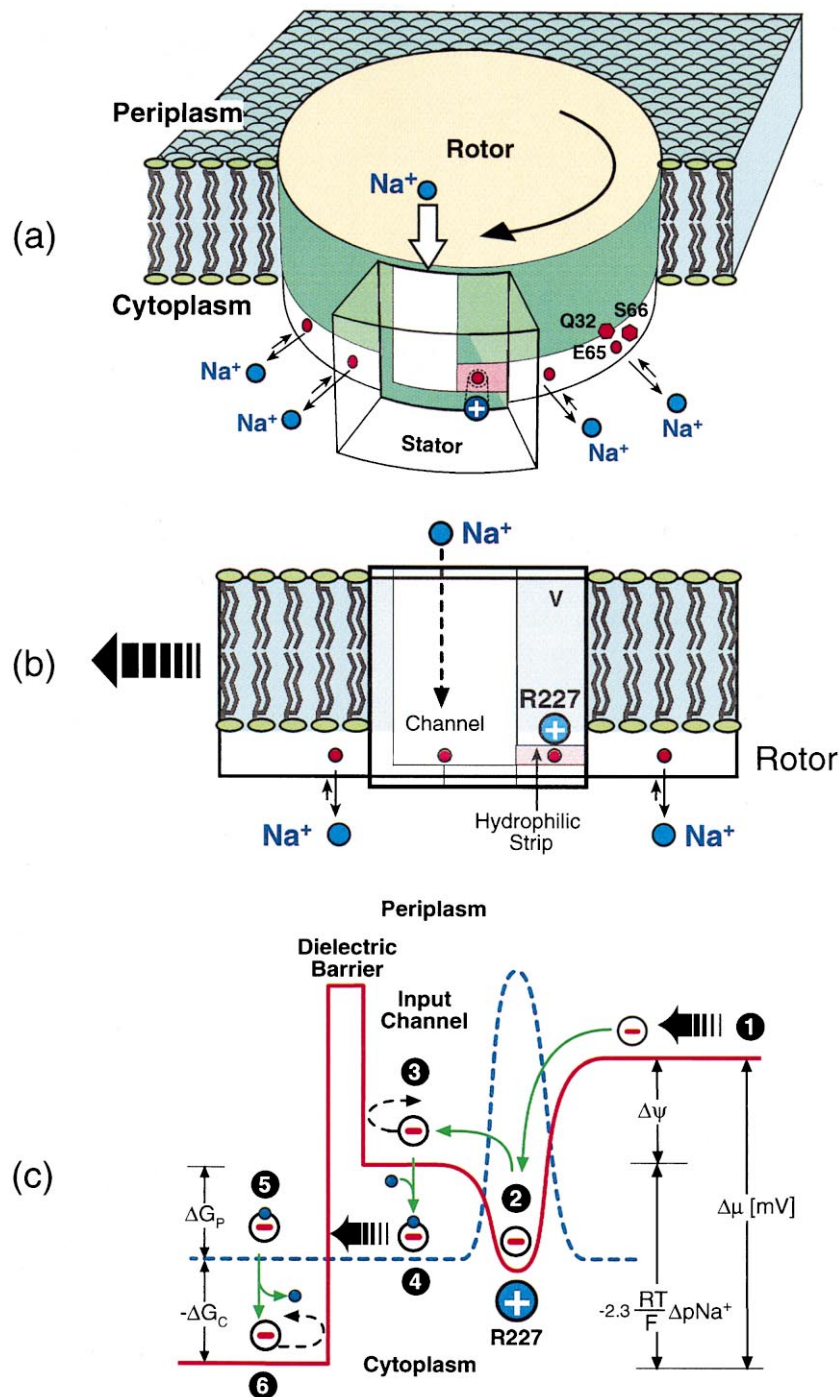
$$\text{pmf} \equiv \frac{\Delta G}{k_B T} = -2.3\Delta pH + \left(\frac{e}{k_B T}\right)\Delta\psi \quad (6)$$

where e is the electronic charge, $\Delta\psi$ is the transmembrane potential, and ΔG is the free energy in units of $k_B T$. However, this equilibrium equation says nothing about how the two components contribute during the non-equilibrium operation; this depends on the mechanism of energy conversion. We will present a model that encompasses most of the known experimental data on the F_o motor, and that fulfills the requirement that it generates the appropriate torque to release nucleotide from the F_1 catalytic sites. Moreover, when supplied with torque from the F_1 motor, it becomes an ion pump. This reversibility is important for bacteria which find themselves in anaerobic conditions, and it supports the strong structural similarities between the F-ATPases and their cousins, the V-ATPase proton pumps.

Modeling the F_o motor presents an entirely different problem from the F_1 motor. First, the atomic

structure of F_o has not been solved, and so structural information is restricted to transmembrane topologies inferred from amino acid sequences for the a and c subunits, and to solution structures inferred from NMR studies. However, mutation experiments have isolated the critical amino acids, and extensive thermodynamic and kinetic studies have determined the energetics and many of the kinetic rates associated with ATP synthesis. Nevertheless, without molecular structures, model building is a more speculative enterprise. We have presented two versions of the F_o motor based on somewhat different inferred structures for the rotor and stator of the proton and sodium driven motors [1,3]. However, the basic operating principle is the same for both, and the mechanochemical performance of both are nearly identical. Here we will base our presentation on the sodium motor of *P. modestum* because additional experimental information is available for it that bears on the role of the membrane potential in torque generation [3,22–26]. A complete account of the mathematical model can be found in the web supplementary material of the above references.

In constructing the F_o motor model we will not exactly parallel our treatment of the F_1 motor since the kinematics and dynamics cannot be as cleanly separated because Brownian motion enters into the dynamics in a much more central and interesting way than in the F_1 motor.



3.1. Geometry of the rotor and the stator

Fig. 10 is a cartoon summarizing a consensus view of the geometry of the counter-rotating a (stator) and c₁₂ (rotor) structures of *P. modestum* [3]. The central features of this organization are:

- There are 12 ion binding sites on the rotor, each consisting of the triplet of charges (Glu65, Gln32, Ser66). The binding sites are located below the level of the membrane, so that sites outside the rotor–stator interface are in equilibrium with the

cytoplasmic reservoir. Mutations at these sites can switch the allegiance of the rotor from sodium to lithium to protons. This means that the rotor site can be treated as a simple Coulomb well.

- There is one critical basic charge on the stator, Arg227, and several polar groups flanking it.
- The pattern of polar groups suggests that the input ion channel penetrates the stator to the lower level of the membrane. Moreover, there is a strip of polar residues on the right side of the channel connecting the lower end of the input channel to the cytoplasm.
- The rotor–stator interface is hydrophobic except for the input channel and the horizontal strip. The hydrophobic interface prevents leakage of ions from the acidic to basic reservoirs. Because of the stator charge, ions cannot pass through the polar strip. However, a rotor site that has not bound a sodium ion can pass into the rotor–stator interface along the strip. A site that has bound an ion is treated as a dipole, and is sufficiently neutralized that it can pass through the hydrophobic interface on the left side of the channel.

Below we will show that the predominant path of ions is to board a rotor site from the input channel, rotate with the rotor site through the hydrophobic region (to the left in Fig. 10), and dissociate into the cytoplasm.

3.2. Dynamics: electrostatic forces and Brownian motion drive the rotor

The rotor and stator interact through Coulomb forces that depend on the ionization state of the rotor sites. Only the sites within and adjacent to the stator affect the rotor motion. Based on the number of α helices constituting the a subunit deduced from the sequence data we assume that the stator spans two rotor sites. Therefore, the rotor–stator interaction is determined by the ionization state of four rotor sites: two sites within the stator and two sites adjacent laterally. Thus the chemical state of the rotor–stator assembly, which we denote as before by s , has $2^4 = 16$ states because each of these four sites may be empty or occupied. Transitions between states occur when an ion binds to or dissociates from a rotor site. Since

the relaxation to equilibrium after an association/dissociation event is much faster than the association/dissociation rates and the mechanical motion, we can treat the transitions between these states as a Markov chain just as before, leading to chemical dynamics similar to Eq. 2. Because of the electrostatic interactions between the rotor sites and the stator charge (Arg227), the transitions between states depend on the angular position of the rotor.

The dynamical equations for the motion of the rotor look formally like Eq. 1; however, the natures of the driving torques are quite different [3]:

$$\zeta \frac{d\theta}{dt} = \underbrace{\tau_Q(\theta, s)}_{\text{Coulomb interaction between rotor and stator charges}} + \underbrace{\tau_{\Delta\psi}(\theta, s)}_{\text{Membrane potential}} + \underbrace{\tau_D(\theta, s)}_{\text{Stator dielectric barrier}} + \underbrace{\tau_{RS}(\theta)}_{\text{Passive interaction between the rotor \& stator}} - \underbrace{\tau_F(\theta)}_{\text{Load torque from } F_l} + \underbrace{\tau_B(t)}_{\text{Brownian torque}}, \quad s = 1, \dots, 16 \quad (7)$$

The torques on the right hand side depend on the rotation angle, θ , and the ionization state of the rotor sites, s :

- $\tau_Q(\theta, s)$ is due to the electrostatic interaction between the stator charge (R227) and the rotor sites that are within or adjacent to the hydrophilic rotor–stator strip. An unoccupied (charged) site will be attracted by the stator charge according to Coulomb's law corresponding to the dielectric and shielding environment of the stator.
- $\tau_{\Delta\psi}(\theta, s)$ is due to the membrane potential drop across the horizontal polar strip connecting the input channel and the stator boundary.
- $\tau_D(\theta, s)$ is the electrostatic barrier that opposes the entry of a charged site into the hydrophobic rotor–stator interface. This barrier arises from difference in dielectric constant between the aqueous channel and the rotor–stator interface. Thus a rotor site must be dehydrated in order to enter the rotor–stator interface, introducing a free energy barrier much larger than $20 k_B T$. This means that the barrier can be treated as essentially infinite since the proton motive force is much smaller than the dielectric barrier.
- $\tau_{RS}(\theta)$ is the passive rotor–stator interaction that arises from the bumpy interface between the rotor and stator and from electrostatic interactions (other than the interaction between the rotor binding sites and the stator charge R227). This interaction

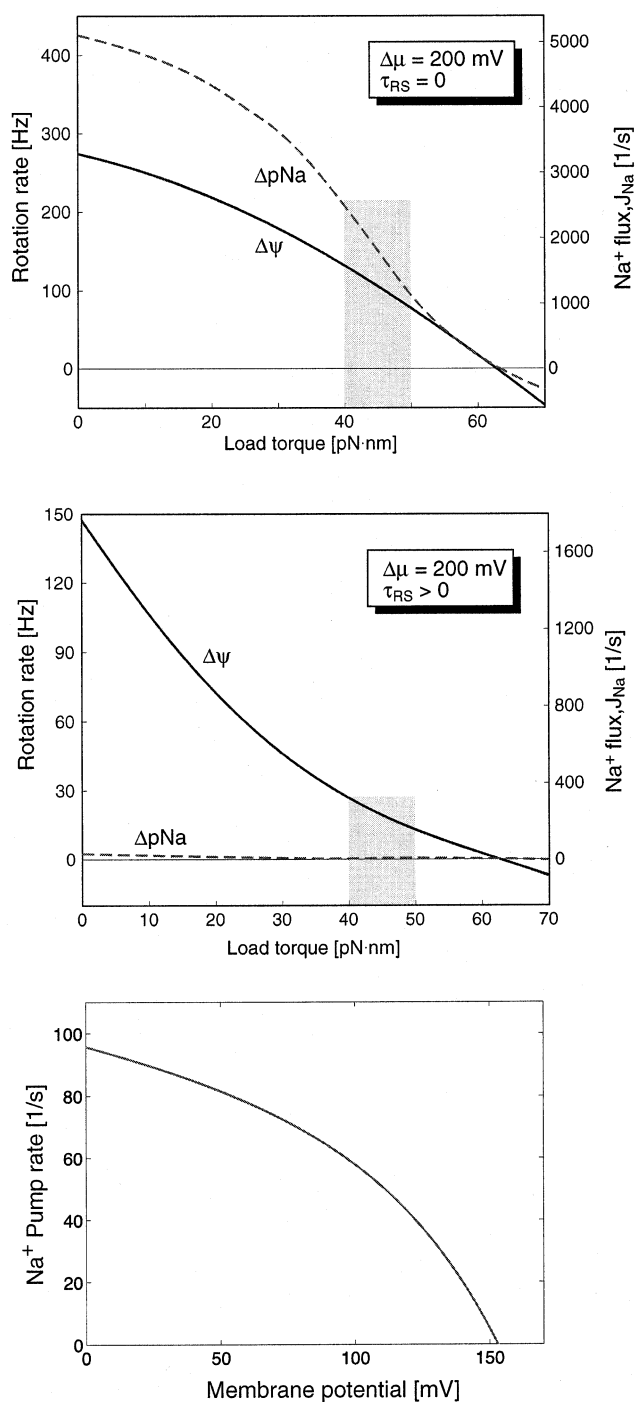


Fig. 11. The performance of the motor and the pump. (a) Load velocity behavior when the passive rotor–stator interaction is small (τ_{RS} in Eq. 7). In this case, the F_o motor produces sufficient torque to generate ATP in F_1 (shaded band). The membrane potential and concentration difference contribute about equally to torque generation near the operating point. (b) Load velocity behavior when the passive rotor–stator interaction, τ_{RS} , is significant. In this situation the requisite torque is provided almost entirely by the membrane potential. This appears to be the case for the *P. modestum* sodium motor. In both (a) and (b), the solid lines are for the case where the motor is driven solely by the membrane potential ($\Delta\psi = 200$ mV, $\Delta pNa = 0$); the dashed lines are for the case where the motor is driven solely by the concentration difference ($\Delta\psi = 0$, $\Delta pNa = 200$ mV). Here the passive interaction potential is chosen to enhance the seizure of negative empty rotor sites by the positive stator charge. Without the help of the membrane potential, empty rotor sites cannot jump out of the potential well. (c) The F_o pump. When the electromotive force is not large enough to counter the torque generated by the F_1 motor, F_o is turned backwards and pumps ions up the electromotive gradient. The curve shows the pump performance as a function of an opposing membrane potential when the sodium concentration is 1 mM on both sides of the membrane. pH regulation by the V-ATPase is discussed in detail in [32].

- $\tau_B(t)$ is the random Brownian torque due to the thermal fluctuations of the rotor.

The quantitative dynamical behavior of the rotor is described by the solutions to Eqs. 2 and 7. We can get a qualitative idea of how the forces and reactions conspire to drive the rotor by examining the potential fields experienced by a rotor site as it passes through the rotor–stator interface. Fig. 10c shows the free energy of a rotor site as it moves through the stator. The figure caption explains how the binding and dissociation of ions to the rotor site switches the electrostatic potential seen by the rotor, which biases the rotor’s diffusion to the left. Note that the potential drop across the polar strip can be viewed as a ‘power stroke’; however, in the absence of rotor diffusion it cannot drive the motor to the left. Rather, it biases the thermal escape of the rotor to the left. In the computations here we have assumed that the input channel is aqueous, so that all of the membrane potential drop occurs across the polar strip. Placing some or all of the potential drop across the input channel increases the effective ion concentration seen by the rotor site, and thus changes the equilibrium binding constant to the rotor sites.

may be required to prevent Brownian fluctuations normal to the interface from allowing ion leakage through the interface.

- $\tau_{F_1}(\theta)$ is the load torque from F_1 opposing the rotor motion. This torque equals to that delivered from F_o to F_1 to power ATP synthesis.

3.3. Coupling F_o and F_1 : the ion turbine and the ion pump

The F_o motor model acts as an ‘ion turbine’ to convert the free energy stored in the transmembrane proton motive force into rotary torque. Does the mechanism we have described generate sufficient torque to synthesize ATP? Before answering this question we must address the issue of how F_o is coupled to F_1 .

As shown in Fig. 9a, the counter-rotating rotor and stator of F_o are coupled through the γ shaft and the b subunits to the rotor and stator of F_1 . If all components were rigid then the stepwise progression of the F_o rotor would be communicated directly to F_1 , and the unbending of the β subunits would take place in steps as well. However, proteins are not rigid bodies, and the coupling between F_o and F_1 is certainly not rigid, for the γ coiled coil has some torsional elasticity and the b_2 stalk that connects the a subunit to the $\alpha_3\beta_3$ hexamer is flexible as well. This elasticity permits much more efficient mechanochemical coupling between F_o and F_1 . The reason is that placing an elastic element between the torque generated in F_o and the load from F_1 smoothes out the rotor steps allowing a nearly constant torque to be delivered to F_1 . Since the most efficient way to transmit energy is via a constant torque (see Appendix A), an elastic coupling between F_o and F_1 is energetically more efficient. Fig. 6c shows the load potential from F_1 seen by the F_o motor. In Appendix C we discuss more generally how elastic coupling affects energy conversion efficiency in ATP synthase.

Fig. 11 shows load velocity curves for two situations: when the *passive* rotor–stator interaction is weak or strong. The top panel shows that when the passive force holding the rotor and stator in register is weak, the F_o motor can generate the 45 pN·nm of torque required to turn F_1 backwards and release newly synthesized ATP from the catalytic site. In this situation, the contributions of the membrane potential ($\Delta\psi$) and the concentration difference (ΔpNa) at the operating conditions are about the same. The middle panel in Fig. 11 shows the situation where the passive rotor–stator interaction is strong. Now the torque is generated almost completely by the membrane potential. This appears to

be the situation in the sodium motor of *P. modestum*, and perhaps in other F_o -ATPases as well [27].

The efficiency of the F_o motor is defined as the ratio of the energy output to the energy consumed. The energy output per step is $\tau_{Load} \times 2\pi/12$. At physiological pH and membrane potential rotation of the motor is tightly coupled to the proton flux. Therefore, the energy consumed per step is given by the proton motive force, $\Delta\mu$. Thus the efficiency is given by the ratio of the energy output per step to the free energy drop per proton passing through the stator: $(\tau_{Load} \times 2\pi/12)/\Delta\mu \sim 70\%$.

3.3.1. The proton F_o motor

The model we have described here was designed to explain the sodium powered F_o motor of *P. modestum*. In an earlier study we described the proton F_o motors of mitochondria and *Escherichia coli* based on a somewhat different geometry [1]. The principle difference between the two motors lies in the location of the rotor sites. The proton F_o model was based on a subunit c structure in which the proton binding sites appeared to be within the membrane spanning region [28,29], whereas in the sodium motor model the sites lie below the level of the membrane, and so are in equilibrium with the cytoplasm. To accommodate this difference the proton F_o rotor was modeled with two half channels rather than one. This requires a proton entering the input channel to board the rotor and ride with it around a complete circuit before dissociating into the exit channel. In the two half channel model for the proton driven motor, we assumed that the membrane potential spans the proton channels in the direction perpendicular to rotor motion [1]. Nevertheless, the two designs (the one half channel model and the two half channel model) operate on the same principle and have the same mechanical properties [3]. The torque generation model cannot distinguish between the mechanical behavior of the one and two channel models because torque is generated at the rotor–stator interface. Therefore, when a proton leaves the interface, whether or not it dissociates or travels a complete circuit before dissociating has no effect on torque generation. However, an important difference between the two models is that the two channel model cannot explain the sodium exchange experiments [30,31]. Yet individual subunits from *E. coli* and

P. modestum can be assembled into functional hybrids. Thus puzzling anomalies remain that must await resolution until an unambiguous structure is available.

Finally, just as the F_1 motor could be driven in reverse to synthesize ATP, the F_o motor can be driven in reverse to perform as an ion pump. Indeed, the closely related V-ATPase proton pumps function in exactly this way [32]. The bottom panel of Fig. 11 shows the performance of the F_o sodium motor as an ion pump when F_1 supplies torque to reverse its rotation direction.

4. Summary: the principles of mechanochemical energy conversion in ATP synthase

In this review we have presented our view of how ATP synthase converts chemical energy into rotational motion. It accomplishes this conversion in two dramatically different ways. The F_1 motor operates at very high mechanochemical efficiency. Thus just as chemical kinetics and thermodynamics place constraints on biochemistry (e.g. detailed balance, overall free energy decrease), so does the high efficiency of F_1 place mechanical constraints on how the free energy of ATP hydrolysis is converted into mechanical force. In particular, this high efficiency requires that the hydrolysis cycle generates a nearly constant torque. Furthermore, the structure of the $\alpha_3\beta_3\gamma$ assembly must couple the conformational changes accompanying nucleotide binding to the rotation of the γ shaft by a tight mechanical escapement that allows few ‘rattles’ or friction that would dissipate energy. To accomplish this the enzyme must bind ATP in a particularly efficient way, which we have called the ‘Binding Zipper’. This requires the binding of ATP to the catalytic site proceeds sequentially, bond by bond, during which the binding energy is converted continuously into bending stress in β . This mechanism permits the catalytic site to generate the required constant mechanical force that drives the power stroke while at the same time storing elastic energy for later release. Finally, synchronization of the hydrolysis cycle with rotation of γ required the equivalent of a camshaft and distributor that could control the angular position of γ at which ATP could gain access to the catalytic site to initiate

the primary power stroke, and later to release phosphate at just the right time to allow the elastic recoil of the secondary power stroke to assist the next catalytic ‘cylinder’ in its primary power stroke. The **Gate 1** and **Gate 2** regions on γ are one way to provide this function, but we have suggested other possibilities as well.

By contrast, the F_o motor is faced with the task of converting energy stored in a transmembrane electrochemical gradient into rotary torque. F_o solves this problem by allowing the ions – protons or sodium – to hop on and off rotating acidic residues and, in so doing, switch the local electrostatic field on and off. Because of the special geometry of the rotor–stator interface, this ‘flashing’ electrostatic field ‘rectifies’ the Brownian motion of the rotor, so that the rotor diffuses predominantly in one direction. When an appreciable membrane voltage is present, the motor takes on a hybrid quality with characteristics of both a Brownian ratchet and a power stroke.

Do these principles generalize to other molecular motors? One is tempted to say yes, because other motors such as kinesin, myosin, and dynein involve nucleotide hydrolysis [33–35]. However, there are several important differences between these motors and F_1 . Most important, F_1 is a rotary engine that does not bind to the γ shaft as it rotates. The linear motors involve a mechanochemical cycle which alternates between strong and weak binding to an actin or microtubule track. For linear motors, energy must be passed between the catalytic and track binding sites. Finally, no linear motor approaches the near 100% efficiency that so constrained our choices in model building, in part because their cycles involve considerable diffusive motions which are absent in F_1 [35–38]. DNA helicases, and RNA polymerase are hydrolysis driven rotary motors, but their structural dissimilarities to F_1 make comparisons difficult [39–41]. So it remains to be demonstrated whether any of the ingredients of the F_1 motor model, such as the Binding Zipper, and the elastic recoil power stroke, are used by other hydrolysis driven motors.

Many questions remain to be answered about the functioning of ATP synthase. For example, what are the structural bases for the ATP and phosphorus gates? All the model can assert is that they are necessary for the motor’s operation.

The F_o motor would appear to be a good para-

digm for the bacterial flagellar motor. Both are rotary engines that can be driven by protons or sodium, and both can be fueled by any combination of ΔpH and a membrane potential. However, there are striking differences which must be resolved before one can extrapolate from F_o to the flagellar motor. First, the flagellar motor generates a far greater torque than F_o ; much more than can be easily accounted for by employing 8–12 stators. Second, the F_o mechanism depended on having a collection of rotating ion bearing sites whose ionization state could implement the diffusion ratchet. Recent mutational work on the flagellar motor suggests that the rotor may not be ionized [42–44]. Finally, the load velocity behavior of the flagellar motor is very different from F_o in ways that are difficult to reconcile [45,46]. All of these obstacles may be overcome eventually, and we may come to see the two as mechanically related in accordance with the view that they are evolutionarily related as well. Or it may be that nature has many tricks up its sleeve when it comes to energy transduction.

Regardless of whether the principles enunciated here extrapolate to other molecular motors, we hope that the methodology we have employed for treating coupled mechanical and chemical processes in motor proteins will prove useful to others.

Acknowledgements

The authors would like to thank Kazuhiko Kinoshita for his insightful comments on the F_1 model, and Peter Dimroth for his collaboration on the sodium F_o motor and for his helpful comments on this manuscript. G.O. and H.W. were supported by NSF Grant DMS-9626104.

Appendix A. Implications of the high mechanical efficiency of F_1

In this appendix we show that a corollary of the high measured efficiency is that the torque generated by the F_1 motor is nearly uniform, independent of the rotational position.

In the experiments carried out by Yoshida and Kinoshita's groups, an isolated $\alpha_3\beta_3\gamma$ hydrolyzed

ATP and drove the rotation of a long actin filament attached to the γ shaft [6,7]. When the ATP concentration was high, the efficiency of the F_1 motor was estimated to be near 100% [6,7,47]. They defined efficiency as the ratio of the 'average energy' dissipated per step (rotation by $2\pi/3$) divided by the hydrolysis free energy of ATP. Thus one concludes that the internal energy dissipation by the F_1 motor must be very small. In other words, *almost all of the ATP hydrolysis free energy goes into generating the torque driving the rotation of the filament*. This statement may appear trivial since the F_1 motor (diameter ~ 10 nm) is very small compared to the filament ($1 \sim 2$ μm) it is driving. Indeed the energy dissipated by the rotating γ shaft alone (excluding the long actin filament) is negligible in comparison with the energy dissipated by the rotating filament.

The key issue raised by this conclusion concerns the mechanical coupling. If ATP hydrolysis is not tightly coupled to the hinge bending of β , and/or the bending motion of β is not tightly coupled to the rotation of the γ shaft, a substantial fraction of the energy will be dissipated to the surrounding fluid. Thus *all moving components of the F_1 motor must be tightly coupled – that is, no rattling about – and the mechanical motions must be tightly coupled to the chemical reaction*.

However, this is not the only conclusion we can draw from the near 100% efficiency. The 'average energy' dissipated per step by the rotating filament was calculated as

$$\Delta E_{\text{EST}}^{\text{Estimated dissipation}} = \zeta_{\text{Drag coefficient}} \cdot \langle \omega \rangle_{\text{Average angular velocity}} \cdot \frac{2\pi}{3} \quad (8)$$

where $\langle \omega \rangle$ is the average of velocity for one motor over long time, or equivalently the average of velocity at one time over an ensemble of motors. Yasuda et al. estimated the efficiency as [6]:

$$\eta \equiv \frac{\Delta E_{\text{EST}}}{-\Delta G_{\text{ATP}}} = \frac{\zeta \langle \omega \rangle \cdot 2\pi/3}{-\Delta G_{\text{ATP}}} \sim 100\% \quad (9)$$

Yasuda et al. fit their data with a simple model that *assumed* a constant torque [6]. Here we demonstrate below by a simple example that Eq. 9 *implies that the torque generated by the F_1 motor is nearly constant, independent of the rotation angle, θ* .

We consider the situation of a horizontal actin

filament rotating around a vertical axis at one end as in the experimental setup [6,7]. The length of the filament is $L = 2.5 \mu\text{m}$, comparable to those used in the experiments. The rotational drag coefficient of the filament, ζ , is given by [48]

$$\zeta = \frac{4\pi}{3} \frac{\eta \cdot L^3}{\log\left(\frac{L}{2r}\right) - 0.447} \quad (10)$$

where $\eta = 10^{-9} \text{ pN}\cdot\text{s}\cdot\text{nm}^{-2}$ is the viscosity of water and $r = 5 \text{ nm}$ is the radius of the filament.

We consider the simple case where the internal dissipation is zero so that all the free energy of ATP hydrolysis goes into driving the rotation of the actin filament. We model this problem as a filament driven by a tilted potential $V_{\text{Drive}}(\theta)$ satisfying

$$V_{\text{Drive}}(\theta) = V(\theta) + \frac{\Delta G_{\text{ATP}}}{2\pi/3} \cdot \theta \quad (11)$$

where $V(\theta)$ is periodic with period $2\pi/3$. That is, the filament is driven by a constant torque $\tau_0 = -\Delta G_{\text{ATP}}/(2\pi/3)$ plus a ‘bump’ potential $V(\theta)$. Here we take $\Delta G_{\text{ATP}} = -23 \text{ k}_B\text{T}$ so that $\tau_0 = 45 \text{ pN}\cdot\text{nm}$. The stochastic motion of the filament is described by a Langevin equation [49]:

$$\underbrace{\zeta \frac{d\theta}{dt}}_{\text{Viscous drag torque}} = \underbrace{\tau_0 - V'(\theta)}_{\text{Driving torque}} + \underbrace{\tau_B(t)}_{\text{Brownian torque}} \quad (12)$$

In the absence of the bump potential (i.e. $V' = 0$), the average angular velocity is

$$\langle \omega_0 \rangle = \frac{\tau_0}{\zeta} \quad (13)$$

The available free energy for driving the filament can be written in terms of $\langle \omega_0 \rangle$ as

$$\Delta G = V_{\text{Drive}}(0) - V_{\text{Drive}}\left(\frac{2\pi}{3}\right) = \tau_0 \cdot \frac{2\pi}{3} = \zeta \langle \omega_0 \rangle \cdot \frac{2\pi}{3} \quad (14)$$

The efficiency defined in [6,47] is given by

$$\eta = \frac{\Delta E_{\text{EST}}}{\Delta G} = \frac{\zeta \langle \omega \rangle \cdot 2\pi/3}{\zeta \langle \omega_0 \rangle \cdot 2\pi/3} = \frac{\langle \omega \rangle}{\langle \omega_0 \rangle} \quad (15)$$

Here $\langle \omega \rangle$ is the average angular velocity in the *presence* of the bump potential, and $\langle \omega_0 \rangle$ is the average

angular velocity in the *absence* of the bump potential. The presence of the bump potential makes the real driving torque uneven. We now show that the bump potential always slows down the average rotation of the filament, i.e. $\langle \omega \rangle \leq \langle \omega_0 \rangle$, and thus reduces the efficiency. Therefore the maximum efficiency can only be attained in the absence of the bump potential, that is, when the driving torque is constant independent of the rotational position.

For the purpose of computing statistical averages of the filament motion one can recast the Langevin equation as an equivalent Fokker–Planck equation. Let $\rho(\theta, t)$ be the probability density that the filament is at the angular position θ at time t . $\rho(\theta, t)$ evolves according to the convection diffusion equation

$$\frac{\partial \rho}{\partial t} = \underbrace{\frac{\partial}{\partial \theta} \left[\frac{1}{\zeta} (V'(\theta) - \tau_0) \rho \right]}_{\text{Convection caused by the driving potential}} + \underbrace{D \frac{\partial^2 \rho}{\partial \theta^2}}_{\text{Brownian diffusion}} \quad (16)$$

where $D = k_B T / \zeta$ is the rotational diffusion coefficient of the filament. Solving equation for the steady state solution with periodic boundary conditions, we obtain that the average angular velocity, $\langle \omega \rangle$, is

$$\langle \omega \rangle = \frac{\frac{\tau_0}{\zeta} \int_0^{2\pi/3} ds \exp\left(\frac{-\tau_0 s}{k_B T}\right)}{\int_0^{2\pi/3} ds \cdot \left[\int_0^{2\pi/3} d\theta \cdot \frac{3}{2\pi} \exp\left(\frac{V(s+\theta) - V(\theta)}{k_B T}\right) \cdot \exp\left(\frac{-\tau_0 s}{k_B T}\right) \right]} \quad (17)$$

The first term of the integrand in the denominator obeys the inequality:

$$\int_0^{2\pi/3} d\theta \cdot \frac{3}{2\pi} \exp\left(\frac{V(s+\theta) - V(\theta)}{k_B T}\right) \geq 1 \quad (18)$$

Therefore $\langle \omega \rangle$ is bounded by $\langle \omega_0 \rangle = \tau_0 / \zeta$ and $\langle \omega \rangle = \langle \omega_0 \rangle$ happens only in the absence of the bump potential (i.e. $V' = 0$).

Fig. 12 shows that the efficiency used by Yasuda et al. decreases as the amplitude of the sinusoidal bump potential increases. Fig. 13 compares a constant torque, a periodic torque, and a Brownian ratchet. This shows that a ratchet with three steps per revolution cannot achieve the measured efficiency. With more steps, the ratchet efficiency increases, but only ap-

proaches that of a constant torque when the number of steps gets very large.

Appendix B. The ‘Binding Zipper’

In Appendix A we have shown that the high efficiency of the F_1 motor required the power stroke to generate a nearly constant torque. In order to accomplish this, we had to assume that when ATP binds to the catalytic site it does so in a progressive fashion that we have called the ‘Binding Zipper’. In this picture, the sequential formation of bonds between ATP and the catalytic site is tightly coupled to the hinge bending motion of β . The initial binding of ATP to the catalytic site is weak, involving only a single bond, or hydrophobic region. The bending motion of β commences with the second bond, and completes after all bonds have been formed, whereupon ATP is bound tightly to the catalytic site. Generally, the weakly bound state of ATP will be short lived because the binding transition from weak to tight happens quickly as other bonds quickly form. When there is little or no resistance to the bending of β , the binding transition proceeds very quickly to the tightly bound state. However, when there is resistance to the bending of β from a load torque, the binding transition can be stopped at an intermediate state by stopping the bending motion of β . Since the bending of β is mechanically coupled tightly to the rotation of γ , stopping rotation should arrest ATP in an intermediate bound state.

During synthesis, the F_0 motor turns γ in the opposite direction and the bending cycle of β is reversed. The bonds holding ATP in place are broken sequentially, and ATP binding affinity is reduced in small steps. Several authors have suggested that the torque generated in F_0 is used to compress a spring, and when the accumulated energy exceeds a threshold, it is used to suddenly spring open the catalytic site [15–17]. However, such a mechanism will dissipate a large portion of the stored elastic energy as the spring recoils. This is very inefficient. Here we compare this idea with the ‘Binding Zipper’ described above.

Because the binding affinity of ATP can change gradually, the interaction between ATP and the catalytic site cannot be described by a two state model:

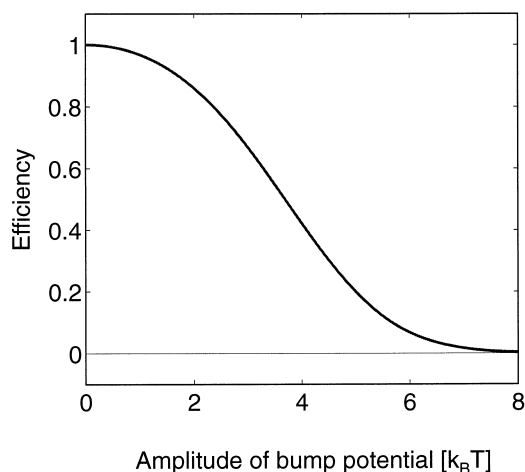


Fig. 12. Efficiency as a function of the amplitude of the bump potential. A filament is driven by a constant torque plus an additional periodic ‘bump’ potential. The ‘efficiency’ is defined as: (average drag torque on the filament \times displacement)/(available free energy). The amplitude of the bump potential measures the deviation of the actual driving torque from a constant torque. This curve demonstrates that the maximum efficiency is achieved when the driving torque is constant.

[bound] \leftrightarrow [unbound]. The binding affinity is directly related to the free energy of the system (ATP+catalytic site). If we model the interaction between the ATP and the catalytic site using a two state model, the binding affinity of ATP will jump from being weakly bound to being tightly bound. This sudden jump in binding affinity corresponds to a sudden jump in the free energy of the system (ATP+catalytic site). In the hydrolysis direction, this sudden jump in free energy is inconsistent with the nearly constant torque of the F_1 motor measured in the experiments [6], since a sudden free energy drop cannot be converted into a constant torque with nearly 100% efficiency. In the synthesis direction, a two state model requires that the energy supply from the F_0 motor be accumulated until enough energy is stored to accommodate a sudden drop in ATP binding affinity. It is not clear how this could be accomplished. It has been proposed that the energy is stored in an elastic spring and then is used to power the ATP binding affinity jump [15–17]. However, after the jump, *most of the energy stored in the spring will be dissipated as the spring recoils*, so this is a dramatically inefficient mechanism.

However, if we allow the ATP binding affinity to change gradually, we can generate a nearly constant

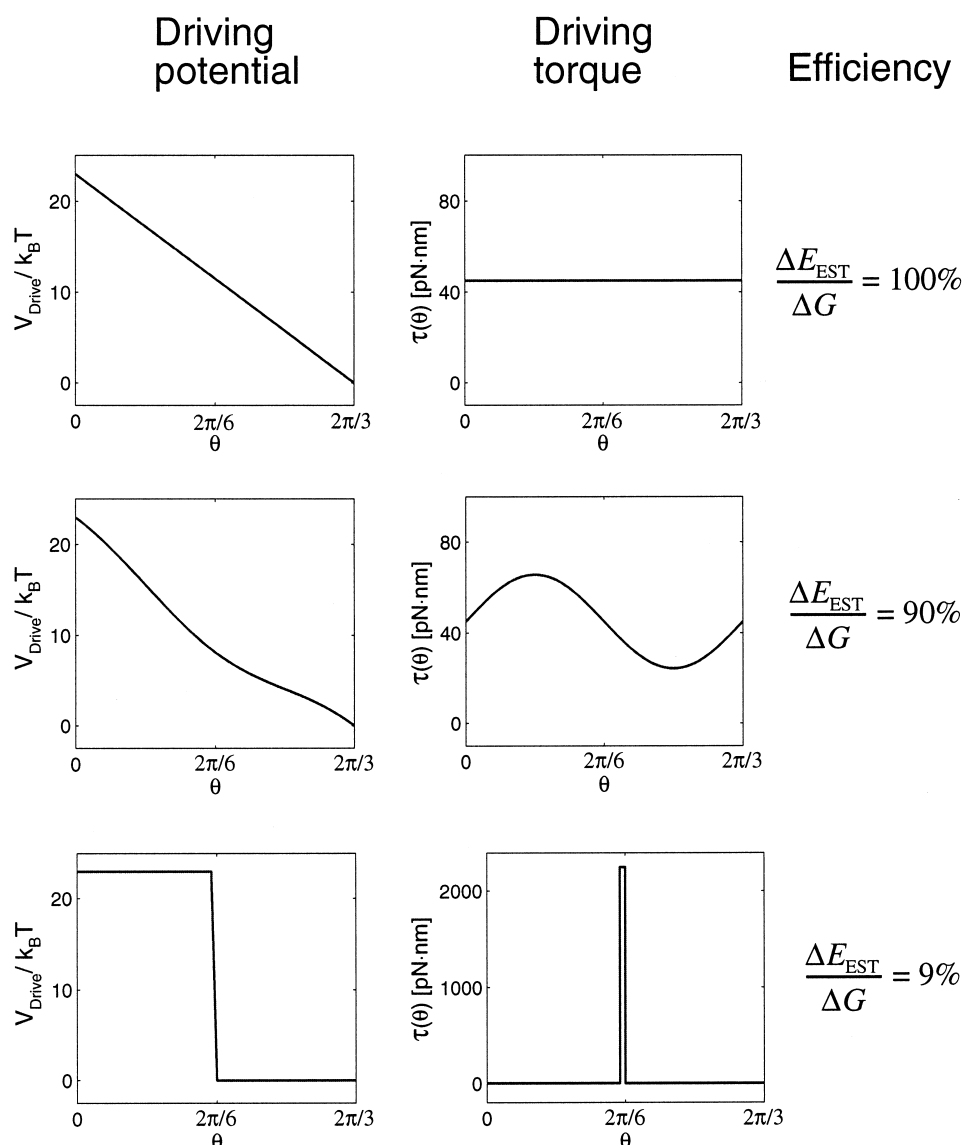


Fig. 13. Comparison of the efficiency for several cases. A filament is driven by potentials (V_{Drive}) shown in the left column. The middle column shows the actual driving torques ($\tau_{Drive} = dV_{Drive}/d\theta$). The right column shows the corresponding efficiencies defined as (average drag torque on the filament \times displacement)/(available free energy). Top row: the filament is driven by a constant torque. Middle row: the filament is driven by a torque with a small periodic amplitude. Bottom row: When the filament is driven by a ratchet, the driving torque is a spike (delta) function, which is very far from a constant torque. Consequently, the efficiency is only $\sim 9\%$.

torque with high efficiency in the hydrolysis direction and release ATP with minimum dissipation in the synthesis direction. In the hydrolysis direction, the binding affinity is increased gradually, bond by bond, so that the free energy of the system is lowered gradually and efficiently to generate a constant torque to drive the rotation of γ . In the synthesis direction, the free energy level of the system (ATP+catalytic site) is raised gradually by the torque supplied

from the F_o motor. The binding affinity of ATP is decreased gradually until thermal fluctuations can dislodge the nucleotide. There is no elastic recoil accompanying release so there is no significant energy dissipation. The Binding Zipper model can be viewed as an extension of Kosland's *Induced Fit* model of enzyme specificity to include the properties that the ligand binds sequentially, and the catalytic site, while flexible, is not too elastic [50].

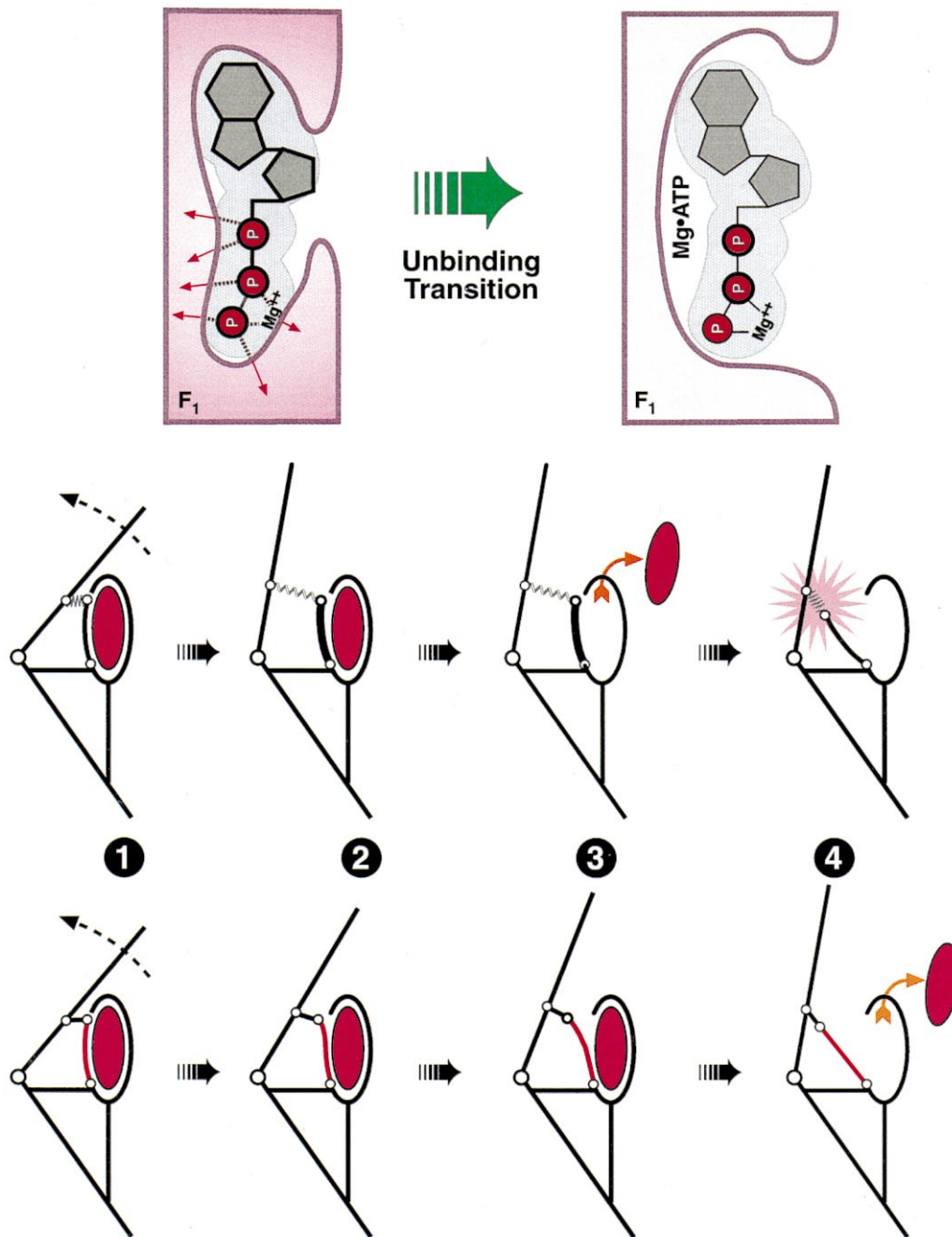


Fig. 14. Comparison of the elastic storage mechanism with the Binding Zipper. Upper panel: Schematic of the unzipping of hydrogen bonds between ATP and the catalytic site during synthesis. Middle panel: The β subunit is represented schematically by two rigid arms connected by a hinge point. The sequence shows the elastic storage mechanism for ATP release [15–17]. The upper arm is connected to the catalytic site by a spring. Driven by the F_0 motor, the bending of β stores elastic energy until it exceeds the level required to free the nucleotide, whereupon the catalytic site springs open. When this happens almost all of the elastic energy stored in the spring is dissipated into heat as the spring recoils to its rest length. Lower panel: The Binding Zipper mechanism. As β bends force is applied uniformly to break the bonds between ATP and the catalytic site sequentially. In this way the ATP binding affinity is reduced gradually by the torque from the F_0 motor. Since the catalytic site is flexible *but not extensible* (like a bicycle chain), little elastic energy is stored during zipping and/or unzipping of these bonds, and consequently little energy is dissipated when bonds form or break.

The middle row of Fig. 14 depicts the process of ATP release proposed in [15–17]. It starts with the ATP tightly bound on the catalytic site. When the top part of β is pushed back by the rotation of the γ shaft it stretches the spring between the β and the catalytic site. The β cannot release ATP until it has accumulated enough energy in the spring. At that point, the stretched spring pulls the catalytic site open, which reduces the ATP binding affinity catastrophically, freeing the ATP from the catalytic site. After the release of ATP, the stretched spring relaxes and a large portion of the elastic energy stored in it is dissipated into heat; thus the process is irreversible and very inefficient.

The bottom row of Fig. 14 describes the Binding Zipper model for ATP release. As before, ATP begins tightly bound in the catalytic site, with all bonds between the nucleotide and the catalytic site in place. As the γ shaft rotates, it bends the top part of β away from the bottom part. This conformational change breaks the bonds one by one and gradually decreases the nucleotide's binding affinity. The second and third panels show intermediate stages where part of the catalytic site has been 'peeled off' from the nucleotide. Note that the connections between the catalytic site and the rest of β are nearly rigid so that little elastic energy is stored in their deformation. That is the catalytic site must be flexible, but not extensible, like a bicycle chain. As the catalytic site is peeled off from the nucleotide, the number of possible bonds that can be formed decreases. Thus the unbending motion of β is directly coupled to decreasing the ATP binding affinity. At the end when all – or nearly all – of the bonds between ATP and the catalytic site are broken, a thermal fluctuation can dislodge the ATP from the catalytic site allowing it to diffuse away. There is little energy dissipated upon ATP release since little elastic energy was stored.

ATP binding is the reverse of this process. Upon the arrival of ATP at the catalytic site (step 4), bond formation between nucleotide and the site commences. As these bonds are being formed one by one, the catalytic site is being pulled closed and the angle between the top part of β and the bottom part closes (steps 3 and 2). When all bonds are formed, the catalytic site is closed and β has completed its bending motion (step 1). Thus the Binding Zipper model predicts that during the ATP binding process, a

nearly constant force is generated utilizing the binding free energy of ATP. For the F_1 motor, part of this force is delivered to drive the rotation of the γ shaft and the rest of it is stored in the β subunit as an elastic energy. This stored elastic energy is released to drive the rotation of the γ shaft when phosphate is released. Thus a constant force is generated and delivered out of the system (ATP+catalytic site) during the ATP binding process. Part of this constant force is delivered to drive the rotation of the γ shaft and the rest of it is stored as elastic energy in the protein structure (β subunit) surrounding the catalytic site.

Finally, we address the question of how the energy stored in the γ phosphate bond of ATP is utilized to sustain the torque generation process. At the end of the ATP binding process, all of the ATP binding free energy has been delivered out of the system (ATP+catalytic site). The free energy of the system has fallen by about $24 k_B T$ and ATP is now tightly bound in the catalytic site at the bottom of a potential well $24 k_B T$ deep. When ATP is hydrolyzed to ADP and phosphate, the tight binding can be destroyed at the expense of the energy stored in the γ phosphate bond. The enthalpic part of the total free energy of ATP hydrolysis is $8\text{--}9 k_B T$, most of which can be attributed to the electrostatic repulsion between the β and γ phosphates.

One likely scenario is that the in-line attack of the water molecule coordinated to βGlu188 in the catalytic site breaks the covalent phosphoanhydride bond on the γ phosphate. This un masks the electrostatic repulsion between ADP and P_i , each of which carries two net negative charges. Since the hydrogen bonds holding the products in the transition state are highly directional, a small misalignment reduces their binding energy significantly. This electrostatic repulsion is sufficient to disorient the hydrogen bonds holding the products in the transition state. In the hydrolysis transition from ATP to ADP and P_i , the free energy of the system (nucleotide+catalytic site) does not change significantly (the equilibrium constant is about 1). The $8\text{--}9 k_B T$ from the electrostatic repulsion between ADP and P_i weakens the total binding from $24 k_B T$ to $15\text{--}16 k_B T$. After hydrolysis, this remaining $15\text{--}16 k_B T$ binding is divided between ADP and P_i so each product is held by a potential well $7\text{--}8 k_B T$ deep. Thermal fluctuations are suffi-

cient to release both products from the catalytic site quickly once the steric block to release (**Gate 2**) is opened. After product release, the next cycle of the reaction can be started. To summarize: in the reaction cycle, the binding transition step generates a torque at the cost of $24 k_B T$ of binding free energy. In the hydrolysis step, $8\text{--}9 k_B T$ is provided electrostatically to switch from the tightly bound ATP state to the loosely bound ADP+ P_i state. The energy for breaking the remaining $15\text{--}16 k_B T$ binding comes endothermically from thermal fluctuations provided by the surroundings in two product release steps, which free the loosely bound ADP and P_i . Such endothermic product release steps are made energetically favorable (rectified) by the entropy increase after the products are released. This entropy increase arises from resonance stabilization of the phosphate, release of a proton, and hydration of the products.

Overall, the free energy level of the system does not change much during the hydrolysis step ($ATP \leftrightarrow ADP \cdot P_i$). In the transition $ATP \rightarrow ADP \cdot P_i$, the γ phosphate bond energy decreases and the binding free energy increases as binding weakens. In the transition $ADP \cdot P_i \rightarrow ATP$, the energy in the γ phosphate bond increases and the binding free energy decreases as binding tightens. The overall free energy change of the system during the transition $ATP \leftrightarrow ADP \cdot P_i$ is small since the equilibrium constant is nearly unity. When the system is in ATP state, ATP is bound tightly in the catalytic site. The major energetic step in synthesis is to use the torque generated in F_o motor to release the tightly bound ATP from the catalytic site.

In the computational model we used a constant force generator that is activated upon ATP docking to model the Binding Zipper [12]. This could be modeled as a pre-stretched spring, which has the same phenomenological behavior as the 'Binding Zipper' because it delivers a nearly constant force over its range of allowed displacements. If all the bonds between the ATP and the catalytic site are similar, it is reasonable to expect that the 'Binding Zipper' generates a nearly constant force during the binding transition. This is surely only approximately true; however, because of Brownian motion within the catalytic site, it is likely that all bonds have about the same average energy.

Appendix C. Does elastic coupling help?

In this section, we investigate the effects of elasticity on the efficiency of delivering mechanical energy. We consider two kinds of mechanical motions: unidirectional motion (e.g. the rotation of F_1 or F_o) and reciprocating motion (e.g. the bending and unbending of β), each of which can be coupled to elasticity in series or in parallel. Thus there are four situations, which are illustrated in Fig. 15.

Fig. 15a shows an elastic element coupling two rotating shafts in *series*. In this situation, the spring acts as an energy buffer, smoothing out variations in the input torque to deliver a nearly constant output torque. The weaker the elastic element, the better the energy buffer. That is, a weak elastic element can take stepwise energy input from one end and output a nearly constant force or torque. Even if the driving torque is very irregular, such as that from a Brownian ratchet, the output torque is nearly constant. Thus an elastic element coupled in series with a unidirectional motion can increase mechanical efficiency.

Fig. 15b shows an elastic element coupled in *parallel* to a *unidirectional* motion. In this situation the motion will wind up the elastic element, increasing the resisting torque until it equals the input torque and the motion ceases. This type of elastic coupling is not relevant for steady state energy transduction because it does not allow a steady state motion.

Fig. 15c shows an elastic element coupled in *series* to a *reciprocating* motion. In this situation the elastic element will alternately store and release elastic energy. However the elastic element decreases rather than increases the efficiency of energy transduction. When the lever moves forward, it first compresses the spring storing elastic energy before commencing to drive rotation of the wheel. However, when the lever reverses its motion, it first allows the compressed spring to recoil releasing its stored energy to drive the motion of the lever. But during this recoil the lever is not driving the motion of the wheel. Consequently the elastic energy released from the spring is dissipated, and makes no contribution to the motion of the wheel. If the lever keeps moving to the left, it will stretch the spring until the spring begins to deliver a pulling force to the driving point on the wheel. However, the elastic energy stored in the stretched spring will be dissipated when the piston reverses its

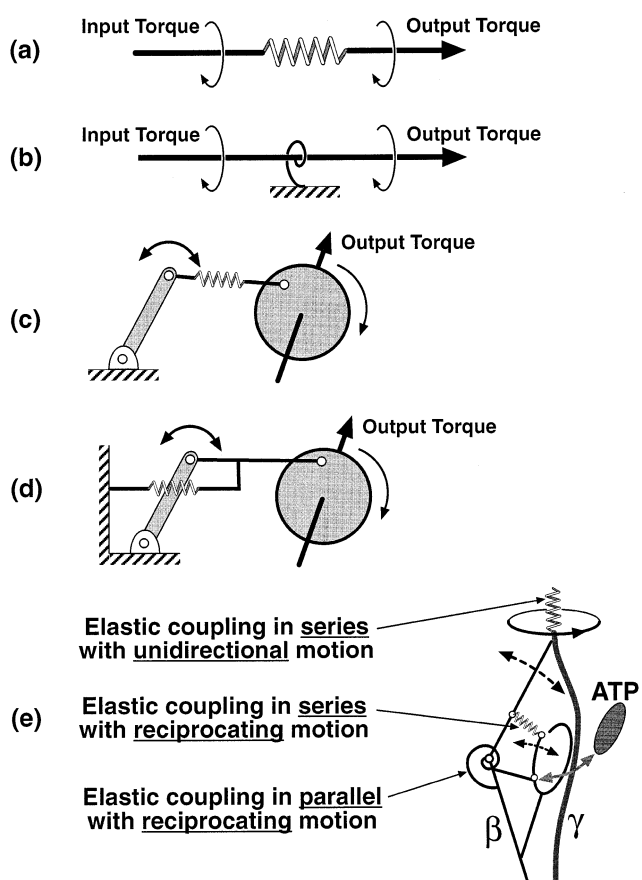


Fig. 15. Four different situations for elastic coupling. (a) Elasticity coupled *in series* to a *unidirectional* motion helps to increase the efficiency. (b) Elasticity coupled *in parallel* to a *unidirectional* motion does not allow a steady state motion. (c) Elasticity coupled *in series* to a *reciprocating* motion decreases the efficiency. (d) Elasticity coupled *in parallel* to a *reciprocating* motion helps to increase the efficiency. (e) Three possible elastic elements involved in the energy transduction of F-ATP synthase.

motion and begins to move to the right again. The weaker the spring, the more the elastic energy is stored in the spring and so the more energy will be dissipated. Thus a weak spring coupled *in series* to a *reciprocating* motion decreases the efficiency of energy transduction.

Fig. 15d shows an elastic element coupled *in parallel* to a *reciprocating* motion. In this configuration the spring alternately stores and releases elastic energy as in the case of series coupling. When the lever moves to the right, it drives the rotation of the wheel and at the same time extends the spring storing elastic energy in it. When the lever reverses, the stretched

spring releases energy to help drive the lever. Since the lever is rigidly connected to the driving point on the wheel, the spring recoil helps to drive the rotation. Thus the elastic element redistributes the energy for driving the reciprocating motion. The elastic element decreases the driving force available for forward motion (storing elastic energy) and increases the driving force available for backward motion. This may or may not increase the efficiency depending on the specific driving force for the reciprocating motion. When the driving force is about the same for both the forward motion and the backward motion, the elastic element will make the driving force uneven and thus decreases efficiency. However, when the driving force for the backward motion is much smaller (or even does not exist, as in a one cylinder gas engine), the elastic element can smooth out the driving force by using the energy stored in forward motion to drive the backward motion and thus increases the efficiency. For macroscopic engines, the job of making the driving force smooth is generally accomplished by a flywheel. However flywheels will not work for molecular motors where inertial forces are negligible.

In Fig. 15e, we identify three possible elastic elements involved in the energy transduction of F-ATP synthase. The spring at the top of the γ subunit represents the torsional elasticity of the γ shaft and the elasticity of the b subunits connecting the rotor and stator of the F_1 and F_0 motors. This spring is coupled *in series* to the *unidirectional* rotation of the γ shaft, so it helps to increase efficiency. The angle spring at the hinge point of the β subunit represents the elasticity of β against its hinge bending motion. Since this spring is coupled *in parallel* to the *reciprocating* motion (opening and closing) of the catalytic site, it also helps to increase the efficiency. The spring connecting the top part of β to the catalytic site represents the protein structure linking the reciprocating motion of the catalytic site to the hinge bending motion of β . Since this spring is coupled *in series* to the *reciprocating* motion of the catalytic site, it decreases efficiency.

Note added in proof

Since submission of the ms. J. Walker's laboratory

has reported a structure for the F_0 subunit of the bovine mitochondrial ATP synthase: Stock, D., Leslie, A. and Walker, J. (1999) *Science* 286, 1700–1705. There they report that the c-rotor consists of 10 subunits, vs. the usually quoted number of 12. This appears to require a non-integer number of protons per ATP-synthesized. However, because of the elastic coupling between F_0 and F_1 , there is no requirement that the number of protons/ATP be integer, and so the principle of operation of the F_0 motor remains unchanged (c.f. Section 3.3 and Appendix C). The Walker laboratory has also found that the ϵ -subunit does not contact the DELSEED sequence on F_1 , as has been previously detected by crosslinking studies. Rather the ‘thumb’ helix region on γ forms hydrogen bonds with DELSEED, and could play the role of the phosphate gate (J. Walker, pers. comm.).

References

- [1] T. Elston, H. Wang, G. Oster, *Nature* 391 (1998) 510–514.
- [2] H. Wang, G. Oster, *Nature* 396 (1998) 279–282.
- [3] P. Dimroth, H. Wang, M. Grabe, G. Oster, *Proc. Natl. Acad. Sci. USA* 96 (1999) 4924–4929.
- [4] P. Boyer, *Biochim. Biophys. Acta* 1365 (1998) 3–9.
- [5] P. Boyer, *Annu. Rev. Biochem.* 66 (1997) 717–749.
- [6] R. Yasuda, H. Noji, K. Kinosita, M. Yoshida, *Cell* 93 (1998) 1117–1124.
- [7] H. Noji, R. Yasuda, M. Yoshida, K. Kinosita, *Nature* 386 (1997) 299–302.
- [8] J. Abrahams, A. Leslie, R. Lutter, J. Walker, *Nature* 370 (1994) 621–628.
- [9] P. Boyer, *Biochim. Biophys. Acta* 1140 (1993) 215–250.
- [10] W. Allison, *Acc. Chem. Res.* 31 (1998) 819–826.
- [11] C.S. Peskin, G.M. Odell, G. Oster, *Biophys. J.* 65 (1993) 316–324.
- [12] H. Wang, T. Elston, A. Mogilner, G. Oster, *Biophys. J.* 74 (1998) 1186–1202.
- [13] A. Senior, *J. Bioenerg. Biomembr.* 24 (1992) 479–483.
- [14] J. Weber, A.E. Senior, *Biochim. Biophys. Acta* 1319 (1997) 19–58.
- [15] Y. Kagawa, T. Hamamoto, *J. Bioenerg. Biomembr.* 28 (1996) 421–431.
- [16] Y. Kagawa, T. Hamamoto, *Biochem. Biophys. Res. Commun.* 240 (1997) 247–256.
- [17] D. Cherepanov, A. Mulikjanian, W. Junge, *FEBS Lett.* 449 (1999) 1–6.
- [18] Y. Shirakihara, A.G.W. Leslie, J.P. Abrahams, J.E. Walker, T. Ueda, Y. Sekimoto, M. Kambara, K. Saika, Y. Kagawa, M. Yoshida, *Structure* 5 (1997) 825–836.
- [19] M. Al-Shawi, C. Ketchum, R. Nakamoto, *J. Biol. Chem.* 272 (1997) 2300–2306.
- [20] M. Al-Shawi, R. Nakamoto, *Biochemistry* 36 (1997) 12954–12960.
- [21] Y. Kato-Yamada, H. Noji, R. Yasuda, K. Kinosita Jr., M. Yoshida, *J. Biol. Chem.* 273 (1998) 19375–19377.
- [22] U. Matthey, G. Kaim, D. Braun, K. Wüthrich, P. Dimroth, *Eur. J. Biochem.*, in press.
- [23] G. Kaim, U. Matthey, P. Dimroth, *EMBO J.* 17 (1998) 688–695.
- [24] G. Kaim, P. Dimroth, *Biochemistry* 37 (1998) 4626–4634.
- [25] P. Dimroth, *Biochim. Biophys. Acta* 1318 (1997) 11–51.
- [26] G. Kaim, F. Wehrle, U. Gerike, P. Dimroth, *Biochemistry* 36 (1997) 9185–9194.
- [27] G. Kaim, P. Dimroth, *EMBO J.*, in press.
- [28] M. Girvin, V. Rastogi, F. Abildgaard, J. Markley, E. Fillin-game, *Biochemistry* 37 (1998) 8817–8824.
- [29] P. Jones, W. Jiang, R. Fillingame, *J. Biol. Chem.* 273 (1998) 17178–17185.
- [30] G. Kaim, P. Dimroth, *EMBO J.* 17 (1998) 5887–5895.
- [31] G. Kaim, P. Dimroth, *FEBS Lett.* 434 (1998) 57–60.
- [32] M. Grabe, H. Wang, G. Oster, *Biophys. J.*, in press.
- [33] R. Vale, R. Fletterick, *Annu. Rev. Cell. Dev. Biol.* 13 (1997) 745–777.
- [34] T. Lohman, K. Thorn, R. Vale, *Cell* 93 (1998) 9–12.
- [35] R. Vale, *J. Cell Biol.* 135 (1996) 291–302.
- [36] E. Sablin, F. Kull, R. Cooke, R. Vale, R. Fletterick, *Nature* 380 (1996) 555–559.
- [37] M.J. Schnitzer, S.M. Block, *Nature* 388 (1997) 386–390.
- [38] C.S. Peskin, G. Oster, *Biophys. J.* 68 (1995) 202s–210s.
- [39] H. Yin, M.D. Wang, K. Svoboda, R. Landick, S.M. Block, J. Gelles, *Science* 270 (1995) 1653–1657.
- [40] M. Wang, M. Schnitzer, H. Yin, R. Landick, J. Gelles, S. Block, *Science* 282 (1998) 902–907.
- [41] M. Hingorani, M. Washington, K. Moore, S. Patel, *Proc. Natl. Acad. Sci. USA* 94 (1997) 5012–5017.
- [42] J. Zhou, S. Lloyd, D. Blair, *Proc. Natl. Acad. Sci. USA* 95 (1998) 6436–6441.
- [43] R. Berry, H. Berg, *Biophys. J.* 76 (1999) 580–587.
- [44] R. Berry, H. Berg, *Biophys. J.* 71 (1996) 3501–3510.
- [45] H. Berg, *Biophys. J.* 68 (1995) 163s–166s.
- [46] H.C. Berg, L. Turner, *Biophys. J.* 65 (1993) 2201–2216.
- [47] S.M. Block, *Nature* 386 (1997) 217–219.
- [48] J. Happel, H. Brenner, *Low Reynolds Number Hydrodynamics: With Special Applications to Particulate Media*, Vol. 1, Nijhoff, The Hague, 1986.
- [49] H. Risken, *The Fokker-Planck Equation*, 2nd Edn., Springer-Verlag, New York, 1989.
- [50] D.E. Koshland, *Proc. Natl. Acad. Sci. USA* 44 (1958) 98–104.
- [51] K. Kinosita, R. Yasuda, H. Noji, M. Yoshida, *Essays Biochem.* 35,